

1994

Tomographic inspection system using X-rays

Vivekanand R. Kini
Iowa State University

Follow this and additional works at: <https://lib.dr.iastate.edu/rtd>

 Part of the [Electrical and Computer Engineering Commons](#)

Recommended Citation

Kini, Vivekanand R., "Tomographic inspection system using X-rays" (1994). *Retrospective Theses and Dissertations*. 237.
<https://lib.dr.iastate.edu/rtd/237>

This Thesis is brought to you for free and open access by the Iowa State University Capstones, Theses and Dissertations at Iowa State University Digital Repository. It has been accepted for inclusion in Retrospective Theses and Dissertations by an authorized administrator of Iowa State University Digital Repository. For more information, please contact digirep@iastate.edu.

Tomographic inspection system using X-rays

by

Vivekanand R. Kini

A Thesis Submitted to the
Graduate Faculty in Partial Fulfillment of the
Requirements for the Degree of
MASTER OF SCIENCE

Department: Electrical Engineering and Computer Engineering
Major: Electrical Engineering

Approved:

In Charge of Major Work

For the Major Department

For the Graduate College

Members of the Committee:

Iowa State University
Ames, Iowa
1994

Copyright © Vivekanand R. Kini, 1994. All rights reserved.

TABLE OF CONTENTS

ACKNOWLEDGEMENTS	x
CHAPTER 1. INTRODUCTION	1
Research Objective	3
Overview of Chapters	4
CHAPTER 2. MATHEMATICAL BACKGROUND	5
Radon Transform	5
Fourier Slice Theorem	6
Filtered Backprojection	9
Backprojection Kernel	13
Fan Projections	14
Fan Beam Filtered Backprojection	15
Displaced Center-of-rotation	21
Simplification	23
Cone Beam Filtered Backprojection	24
CHAPTER 3. SETUP	28
Generator	28
Positioning Control	30
Image Intensifier	31

Camera	32
Frame Grabber	33
DSP Board	33
Network Connection	33
CHAPTER 4. IMPLEMENTATION	35
Data Acquisition	35
X-ray Physics	35
Acquiring Projection	36
Sampling Interval	38
Alignment	41
Center of Rotation	43
Stepping through Fan Beam Reconstruction	45
Cone Beam 3D Reconstruction	51
Performance Improvement	54
Gray Scale Subranging	54
Noise	55
Equalization	58
Smoothing	64
Polychromaticity	67
Implementation Flow	69
CHAPTER 5. RESULTS	73
Casting Inspection	73
Inspection of Cracks	75
Packing Density	75

CHAPTER 6. CONCLUSIONS AND FUTURE WORK	80
Conclusions	80
Future Work	81
Dynamic Range Expansion	81
Inspecting Objects Larger than Field of View	81
Camera Mount	82
Distributed 3D Reconstruction	83
Integrated System	83
BIBLIOGRAPHY	84

LIST OF FIGURES

Figure 1.1:	Computed tomography is distinguished from conventional radiography by the different orientation of the image plane . . .	3
Figure 2.1:	Projection of an object	6
Figure 2.2:	Fourier slice theorem	8
Figure 2.3:	Location of estimates of fourier transform	9
Figure 2.4:	Idea behind filtered backprojection	10
Figure 2.5:	Ideal filter response for filtered backprojection	13
Figure 2.6:	Fan beam projection	15
Figure 2.7:	Projection parameters for equispaced collinear detectors . . .	17
Figure 2.8:	Parameters used in derivation of reconstruction algorithm . .	18
Figure 2.9:	Parameters used for calculation of U and s'	19
Figure 2.10:	Fan beam geometry with displaced center-of-rotation	22
Figure 2.11:	Rotated coordinate system (p, q)	23
Figure 2.12:	Cone beam reconstruction from tilted fans	25
Figure 2.13:	Coordinate system for tilted fan	26
Figure 3.1:	System setup	29
Figure 3.2:	Motion control	31

Figure 3.3:	Image intensifier	32
Figure 4.1:	Lambert's Law (a) One dimensional case (b) Two dimensional case	36
Figure 4.2:	Test sample	39
Figure 4.3:	Sinogram	39
Figure 4.4:	Slice for calculating the sampling interval a	40
Figure 4.5:	Misalignment	42
Figure 4.6:	Projections for calculating center of rotation (a) Projection at 0° (b) Projection at 180°	43
Figure 4.7:	Center of rotation calculation	44
Figure 4.8:	Reconstruction steps (a) Slice (b) Projection (c) Weighted projection (d) Smoothed projection (e) Filtered projection . .	49
Figure 4.9:	Time Domain (a) Backprojection kernel (b) Hamming window	50
Figure 4.10:	Frequency response (a) Backprojection kernel (b) Hamming window	50
Figure 4.11:	(a) Image after 1 Backprojection (b) Final image 320 back- projections	52
Figure 4.12:	Simplified schematic of digitization process	55
Figure 4.13:	Gray scale subranging	56
Figure 4.14:	Noise against frames averaged	57
Figure 4.15:	Noise against frames averaged for different levels of gray scale subranging: 8(Dotted), 4(dashed), 1(Solid)	58
Figure 4.16:	Reconstructed image after frame averaging	59

Figure 4.17:	Dotted line is the background slice; Solid line passing through it shows the smoothed slice; Other solid line shows noise pattern which is offset for ease of viewing	60
Figure 4.18:	Patterns representing CCD noise	61
Figure 4.19:	Background slices used for pixel response characterization . .	62
Figure 4.20:	Pixel response characteristics plotted for pixel numbers 10, 100, 250, 400, 550, 630	63
Figure 4.21:	Reconstructed image after pixel response equalization	64
Figure 4.22:	Filtered projections after varying choice of hamming window for smoothing (a) none (b) 4 (c) 10 (d) 20	65
Figure 4.23:	Reconstructed images after varying choice of hamming window for smoothing (a) none (b) 4 (c) 10 (d) 20	66
Figure 4.24:	(a) Projection with zero padding (b) Filtered projection after zero padding (c) Projection with smooth padding (d) Filtered projection after smooth padding	68
Figure 4.25:	Bremsstrahlung spectrum from a X-ray generator	69
Figure 4.26:	Spectrum of filtered beam from a X-ray generator	70
Figure 4.27:	Flowchart	71
Figure 5.1:	(a) Aluminum casting (b) Image from the realtime system (c) Reconstructed image	74
Figure 5.2:	Slices across a 3D tomogram of aluminum casting	76
Figure 5.3:	(a) Fatigue crack sample (b) Image from the real-time system (c) Reconstructed image (d) Crack (zoomed)	77
Figure 5.4:	Slices across a 3D tomogram of fatigue crack	78

ACKNOWLEDGEMENTS

Thank you Joe for your guidance, trust, support and enthusiasm. By working under you, I have been enriched with an experience which will go a long way in guiding me in all my future endeavors.

Thank you Dick, Terry, Lalita Udpa, Satish Udpa and Kelvin Nilsen for your guidance. My work at CNDE has been very memorable and enjoyable experience, thanks to Sarat, Jason, Liz, Tahir, Ranga, Simon, Deven and many others.

Words cannot capture my gratitude to my parents. Thank you mummy, pappa, munna, nani and mamai for standing by me. I could have never made it so far in life without the feeling of solid security, love and trust which you provide. Also, thank you Neeta, Avadhut, Medha, Shailesh, Reeta pacchi,... and so many other relatives and acquaintances for your support and all the good times we had together.

Thank you Sriram for a great friendship and to you I attribute all my programming skills. Thank you Amarnath, Rashmi, Shiv, Sunil, Chondo, ... and many others for bearing with me and making me feel at home so far away from home. Thank you Deepak, Yeshwant and Kim for the memorable and educating experience at SJCE. Last but not the least, thank you Michelle (my car) for being so reliable and for the fabulous drives across this country.

CHAPTER 1. INTRODUCTION

Tomography refers to the cross-sectional imaging of an object from either transmission or reflection data collected by illuminating the object from many different directions. This technique revolutionized diagnostic medicine since it enabled doctors to view the slices of internal organs of the patient using x-rays. For the same reason, the method is being used in industry for applications such as inspection of turbine blades, rocket motors, ceramics, electronic components, castings, etc.

The mathematical basis of CT was established by J.Radon [1] in 1917 when he showed that it is possible to determine the value of a function over a region of space if the set of line integrals is known for all ray paths through the region. In the case of CT, the line integrals are derived from the x-ray intensities sensed by the detectors, and the function to be determined is the distribution of the x-ray attenuation coefficient over the object. However, the large number of calculations needed to accomplish the reconstruction ruled out any practical application to x-ray data until the availability of relatively rapid computers. Hounsfield and Cormack first received a nobel prize in 1979 in medicine for their x-ray brain scanner with reconstruction time of 2 days. Since then several advances have been made resulting in fast reconstruction algorithms. Fourier weighted backprojection developed by Ramchandran and Laxminarayan is one of the most commonly used algorithm. This algorithm bring

out the splendor and power of mathematical formulation of a problem. With very few assumptions, cross-sectional view of an object can be obtained with unprecedented accuracy. The amount of computation involved is still complex enough to demand considerable computing power.

A variety of applications have arisen in recent years for nondestructive evaluation (NDE) and testing. X-ray radiography is one of the most widely used techniques for NDE. In conventional radiography, the image plane is approximately normal to the x-ray beam and the image represents the total x-ray attenuation coefficient μ through the object. The CT method creates a digital representation of a thin slice parallel to the x-ray beam. This difference is highlighted in Figure 1.1. The advantage is that the image data represents a local material-dependent property, the linear attenuation coefficient, that is largely independent of the object geometry. Conventional radiography only represents an integral of μ along the x-ray path through the object. Thus, a major limitation of radiography, the inability to distinguish between thickness and density changes, is overcome by CT, providing more useful and quantitative characterization of materials.

To meet demands of sensitivity, resolution and especially of speed, most of the industrial CT systems are large and expensive. The detector array used to collect full projections with high resolutions represent an effective way to achieve speed and image quality. However, there are a large number of applications where the dimensional information, especially in the part interior is needed that doesn't require the high quality images typically obtained from industrial CT systems. Inexpensive systems having a measure of speed have a definite niche. X-ray inspection systems employing real time detectors such as image intensifiers, scintillation glass, etc have an

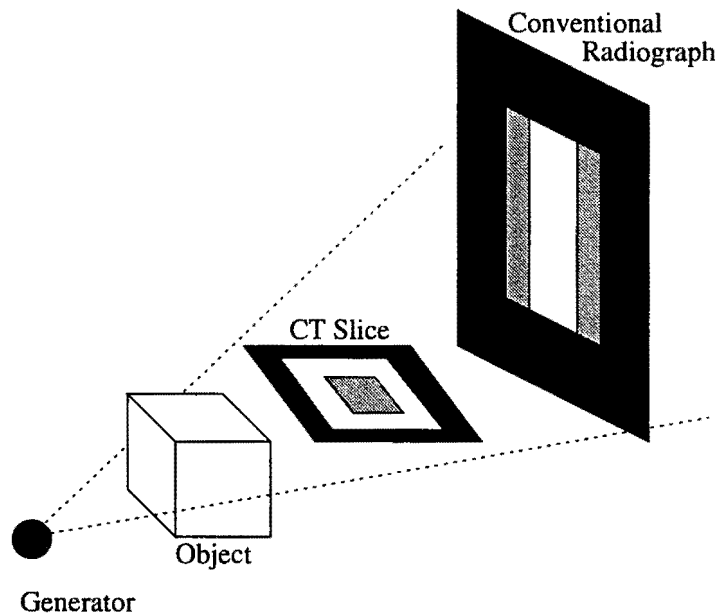


Figure 1.1: Computed tomography is distinguished from conventional radiography by the different orientation of the image plane

advantage of speed and are much less expensive than the traditional scintillation array detectors. The trade-off is the loss of signal dynamic range, low spatial resolution and the introduction of detector systematics into the signal.

Research Objective

The objective of this thesis is to develop a fast and relatively cheap system for quick tomographic inspection by using an available real time radiography setup.

Overview of Chapters

Chapter 2 lays the mathematical foundations for computed tomography. Chapter 3 describes the real-time radiographic inspection setup. A brief overview of the various equipment used is given. Chapter 4 describes the implementation details. It steps through the data acquisition and reconstruction process and various issues which arise during implementation. Also, the system limitations and various methods of improving the system capability are discussed. Chapter 5 deals with details about the programming model used. A brief description of various possible application areas is done in Chapter 6. Finally we conclude with the possible future work with Chapter 7.

CHAPTER 2. MATHEMATICAL BACKGROUND

This chapter describes the mathematical basis of tomography with nondiffracting sources. It starts with Radon transform which relates the line integrals to the projections of an object. By finding the Fourier transform of the projection taken along parallel lines, Fourier Slice Theorem is derived. This theorem acts as the key to tomographic imaging by relating the measured projection data to the two-dimensional Fourier transform of the object cross section. Fourier Backprojection algorithm is then derived by mathematical manipulation of this theorem and extended to the case of fan beam projection with equispaced collinear detector elements. The result is then simplified and generalized to three dimensional cone beam reconstruction. Also, some of the issues concerning computer implementation are addressed.

Radon Transform

Let an object be specified by two dimensional function $f(x, y)$ and each line integral by (θ, t) parameters as shown in Figure 2.1. The equation of line AB is

$$x \cos \theta + y \sin \theta = t \quad (2.1)$$

The projection $P_\theta(t)$ can be represented as the line integral:

$$P_\theta(t) = \int_{(\theta, t) \text{ line}} f(x, y) ds$$

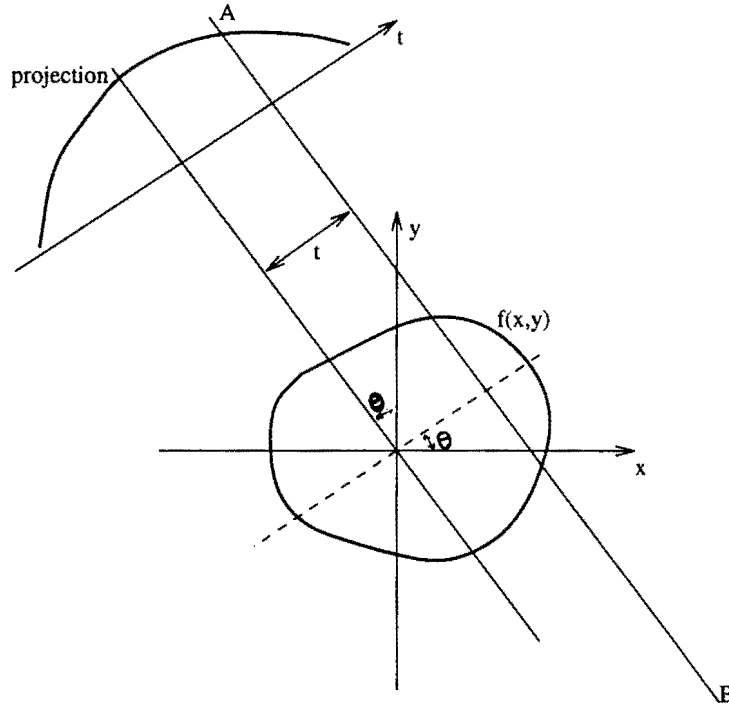


Figure 2.1: Projection of an object

$$= \int_{-\infty}^{\infty} \int_{-\infty}^{\infty} f(x, y) \delta(x \cos \theta + y \sin \theta - t) dx dy \quad (2.2)$$

$P_{\theta}(t)$ is called the *Radon Transform* of function $f(x, y)$.

Fourier Slice Theorem

A two dimensional Fourier transform of the object function $f(x, y)$ can be defined as

$$F(u, v) = \int_{-\infty}^{\infty} \int_{-\infty}^{\infty} f(x, y) e^{-j2\pi(ux+vy)} dx dy \quad (2.3)$$

The Fourier transform of projection $P_{\theta}(t)$ at angle θ can be defined as

$$S_{\theta}(\omega) = \int_{-\infty}^{\infty} P_{\theta}(t) e^{-j2\pi\omega t} dt \quad (2.4)$$

the (t, s) coordinate system can be considered to be a rotated version of (x, y) system as expressed by

$$\begin{bmatrix} t \\ s \end{bmatrix} = \begin{bmatrix} \cos \theta & \sin \theta \\ -\sin \theta & \cos \theta \end{bmatrix} \begin{bmatrix} x \\ y \end{bmatrix} \quad (2.5)$$

In the (t, s) coordinate system, a projection along lines of constant t is written as

$$P_\theta(t) = \int_{-\infty}^{\infty} f(t, s) ds \quad (2.6)$$

Substituting this into 2.4 gives

$$S_\theta(\omega) = \int_{-\infty}^{\infty} [f(t, s) ds] e^{-j2\pi\omega t} dt \quad (2.7)$$

Using equation 2.5, this result can be transformed into (x, y) coordinate system

$$S_\theta(\omega) = \int_{-\infty}^{\infty} \int_{-\infty}^{\infty} f(x, y) e^{-j2\pi\omega(x \cos \theta + y \sin \theta)} dx dy \quad (2.8)$$

The RHS represents the two-dimensional Fourier transform of $f(x, y)$ at spatial frequency of $(u = \omega \cos \theta, v = \omega \sin \theta)$ or

$$S_\theta(\omega) = F(\omega, \theta) = F(\omega \cos \theta, \omega \sin \theta) \quad (2.9)$$

This equation is the essence of *Fourier Slice Theorem* which can be stated as [9]

The Fourier transform of a parallel projection of an image $f(x, y)$ taken at angle θ gives a slice of the two-dimensional transform, $F(u, v)$, subtending an angle θ with the u -axis. In other words, the Fourier transform of $P_\theta(t)$ gives the values of $F(u, v)$ along line BB in Figure 2.2.

Thus, if infinite number of projections are taken, then $F(u, v)$ would be known at all the points in the (u, v) plane. Knowing $F(u, v)$, the object $f(x, y)$ can be recovered as

$$f(x, y) = \int_{-\infty}^{\infty} \int_{-\infty}^{\infty} F(u, v) e^{j2\pi(ux+vy)} du dv \quad (2.10)$$

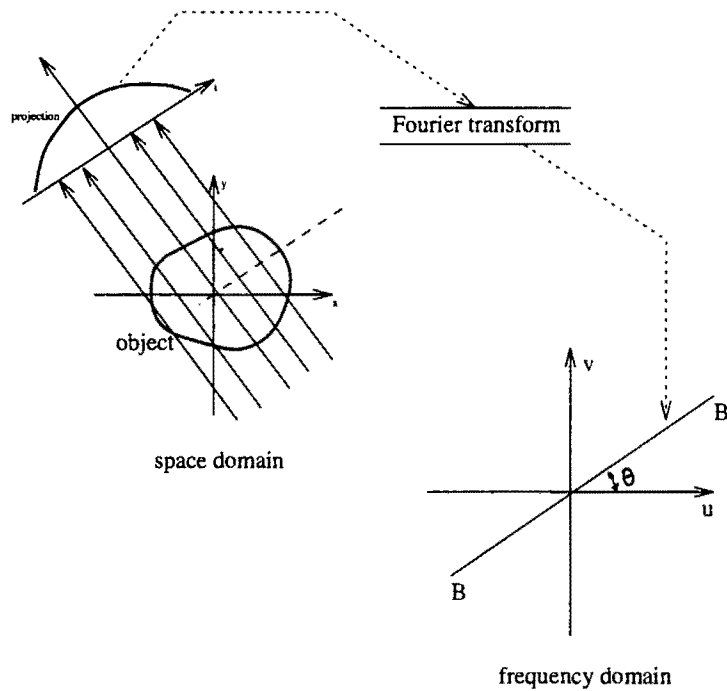


Figure 2.2: Fourier slice theorem

In practice, only a finite number of projections can be taken, which gives estimates of $F(u, v)$ along radial lines as shown in Figure 2.3. The dots represent the actual location of the estimates since implementation is done in discrete domain. Thus to use equation 2.10, one must interpolate from these radial points on to a square grid. Since the density of radial points becomes sparser as one gets away from the center, the interpolation error becomes larger. This implies that there is greater error in the calculation of the high frequency components in an image than in the low frequency ones.

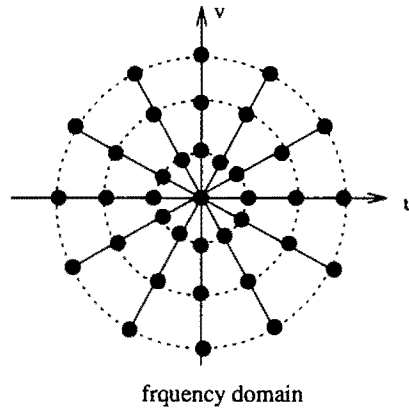


Figure 2.3: Location of estimates of fourier transform

Filtered Backprojection

In this section, we discuss a method of interpolation in frequency domain. This idea can be visualized in Figure 2.4. The projection data measured gives us the Fourier transform along a straight radial line (equation 2.9) as shown in Figure 2.4(b). To apply equation 2.10, we need a pie-slice of Fourier transform as shown in Figure 2.4(a) because we have to cover the entire Fourier frequency domain. The filtered backprojection method takes the measured data in Figure 2.4(b) and applies the weighing in the frequency domain as shown by Figure 2.4(c) so that the data in Figure 2.4(b) is an approximation of that in Figure 2.4(a). The weighing function shown in Figure 2.4(c) constitutes the filter and hence the name *filtered projection*. It can be seen that the filter in Figure 2.4(c) is nothing but a high pass filter.

In equation 2.10, exchanging rectangular coordinate system in frequency domain (u, v) with polar coordinate system (ω, θ) by substituting

$$u = \omega \cos \theta$$

$$v = \omega \sin \theta$$

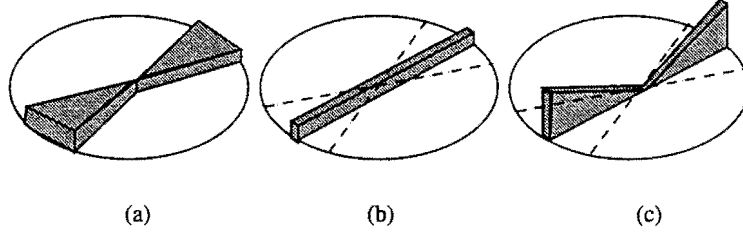


Figure 2.4: Idea behind filtered backprojection

$$du dv = \omega d\omega d\theta$$

we can write

$$f(x, y) = \int_0^{2\pi} \int_0^{\infty} F(\omega, \theta) e^{j2\pi\omega(x \cos \theta + y \sin \theta)} \omega d\omega d\theta \quad (2.11)$$

This line integral can be split into two by considering θ from 0° to 180° and then from 180° to 360° .

$$f(x, y) = \int_0^{\pi} \int_0^{\infty} F(\omega, \theta) e^{j2\pi\omega(x \cos \theta + y \sin \theta)} \omega d\omega d\theta + \int_0^{\pi} \int_0^{\infty} F(\omega, \theta + 180^\circ) e^{j2\pi\omega(x \cos(\theta+180^\circ) + y \sin(\theta+180^\circ))} \omega d\omega d\theta \quad (2.12)$$

Since $F(\omega, \theta + 180^\circ) = F(\omega, -\theta)$

$$f(x, y) = \int_0^{\pi} \left[\int_{-\infty}^{\infty} F(\omega, \theta) |\omega| e^{j2\pi\omega t} d\omega \right] d\theta \quad (2.13)$$

where $t = x \cos \theta + y \sin \theta$ for simplicity. Now, by using Fourier Slice Theorem (2.9), we get

$$f(x, y) = \int_0^{\pi} \left[\int_{-\infty}^{\infty} S_{\theta}(\omega) |\omega| e^{j2\pi\omega t} d\omega \right] d\theta \quad (2.14)$$

This can be expressed as

$$f(x, y) = \int_0^{\pi} Q_{\theta}(x \cos \theta + y \sin \theta) d\theta \quad (2.15)$$

where

$$Q_\theta(t) = \int_{-\infty}^{\infty} S_\theta(\omega) |\omega| e^{j2\pi\omega t} d\omega \quad (2.16)$$

This equation represents the filtering operation of the projection data transform $S_\theta(\omega)$, where the frequency response of the filter is given by $H(\omega) = |\omega|$; therefore $Q_\theta(\omega)$ is called the *filtered projection*. By the convolution theorem, 2.16 can be rewritten as

$$Q_\theta(t) = \int_{-\infty}^{\infty} S_\theta(\omega) H(\omega) e^{j2\pi\omega t} d\omega \quad (2.17)$$

$$= \int_{-\infty}^{\infty} P_\theta(t') h(t - t') dt' \quad (2.18)$$

where

$$h(t) = \int_{-\infty}^{\infty} |\omega| e^{j2\pi\omega t} d\omega \quad (2.19)$$

The resulting projections from different angles θ are then added to form an estimate $f(x, y)$ as is represented in 2.15. The filtered projection Q_θ will make the same contribution to the reconstruction of all the points along constant t where $t = x \cos \theta + y \sin \theta$. Therefore, one could say that in the reconstruction process each filtered projection, Q_θ , is smeared back or *backprojected* over the image plane and hence the name *filtered backprojection*. We can now summarize by writing the object ($f(x, y)$) as

$$f(x, y) = \frac{1}{2} \int_0^{2\pi} \int_{-\infty}^{\infty} P_\theta(t) h(x \cos \theta + y \sin \theta - t) dt d\theta \quad (2.20)$$

The next step is to discretize equation 2.20 by approximating the integrals with the summation. Assuming that W is the highest frequency component in each projection, then by the Nyquist criterion [7] the projections can be sampled at intervals of a where

$$a = \frac{1}{2W} \quad (2.21)$$

If the projection data are equal to zero for larger values of t then a projection can be represented as

$$P_\theta(nT), \quad n = -\frac{N}{2}, \dots, 0, \dots, \frac{N}{2} - 1 \quad (2.22)$$

An FFT algorithm can then be used to approximate the Fourier transform of the projection by

$$S_\theta(\omega) \approx S\left(n\frac{2W}{N}\right) = \frac{1}{2W} \sum_{k=-N/2}^{N/2-1} P_\theta\left(\frac{k}{2W}\right) e^{j2\pi(nk/N)} \quad (2.23)$$

This is shown in Figure 2.3. The filtered projection is then calculated as

$$Q_\theta\left(\frac{k}{2W}\right) \approx \left(\frac{2W}{N}\right) \sum_{k=-N/2}^{N/2-1} S_\theta\left(n\frac{2W}{N}\right) \left|n\frac{2W}{N}\right| e^{j2\pi(nk/N)} \quad (2.24)$$

Since the filter is a high pass filter, high frequency noise that may be present in the projection gets highly amplified. Therefore, from the standpoint of noise in the reconstructed image, superior results are obtained if one multiplies the filtered projection by a smoothing function $H(m(2W/N))$ (such as a Hamming window)

$$Q_\theta\left(\frac{k}{2W}\right) \approx \left(\frac{2W}{N}\right) \sum_{k=-N/2}^{N/2-1} S_\theta\left(n\frac{2W}{N}\right) \left|n\frac{2W}{N}\right| H\left(m\frac{2W}{N}\right) e^{j2\pi(nk/N)} \quad (2.25)$$

The reconstructed picture may then be obtained by the discrete approximation to the integral in 2.15

$$f(x, y) = \frac{\pi}{K} \sum_{i=1}^K Q_{\theta_i}(x \cos \theta_i + y \sin \theta_i) \quad (2.26)$$

where the K angles θ_i are those for which the projections $P_\theta(t)$ are known.

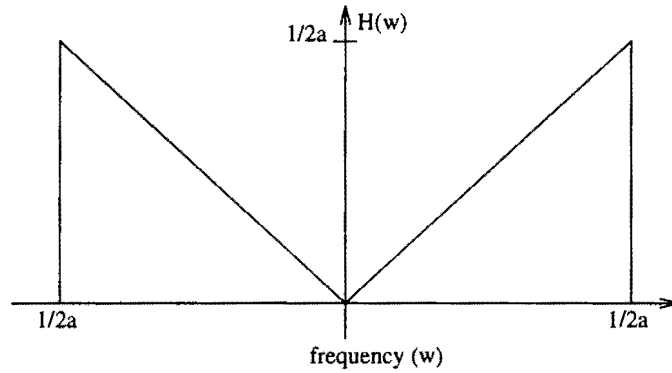


Figure 2.5: Ideal filter response for filtered backprojection

Backprojection Kernel

In this section we discuss the issue facing the implementation of the backprojection kernel. The ideal response of the backprojection filter is as shown in Figure 2.5. The discretized implementation of equation 2.26 *zeroes out* all the information in the continuous frequency domain in the cell represented by $n = 0$, whereas the theory (equation 2.16) calls for such *zeroing out* to occur only at one frequency, viz. $\omega = 0$. This results in dishing artifacts in the reconstructed image which is removal of the low frequency components. This effect can be reduced by zero-padding projections in the space domain which causes the cell size to get smaller in the frequency domain. However, it can be eliminated by the following alternative implementation. When the highest frequency in the projections is finite, the frequency response of the backprojection filter can be expressed as

$$H(\omega) = |\omega|b_{\omega}(\omega) \quad (2.27)$$

where

$$b_{\omega}(\omega) = \begin{cases} 1 & |\omega| < W \\ 0 & \text{otherwise} \end{cases} \quad (2.28)$$

The impulse response, $h(t)$ of this filter is given by the inverse Fourier transform of $H(\omega)$ and is

$$\begin{aligned} h(t) &= \int_{-\infty}^{\infty} H(\omega) e^{j2\pi\omega t} d\omega \\ &= \frac{W \sin 2\pi t W}{\pi t} - \left(\frac{\sin \pi t W}{\pi t} \right)^2 \\ &= \frac{1}{2a^2} \frac{\sin 2\pi t/2a}{2\pi t/2a} - \frac{1}{4a^2} \left(\frac{\sin \pi t/2a}{\pi t/2a} \right)^2 \end{aligned} \quad (2.29)$$

The backprojection kernel can then be given by

$$h(na) = \begin{cases} 1/4a^2, & n = 0 \\ 0, & n \text{ even} \\ -\frac{1}{n^2\pi^2 a^2}, & n \text{ odd} \end{cases} \quad (2.30)$$

Fan Projections

The preceding discussion dealt with reconstructing images from their parallel projections. In generating these parallel data, the object has to be linearly scanned over the length of a projection, then rotated through a certain angular interval, then scan linearly over the length of the next projection, and so on. This is usually very costly in terms of time. It is suited for the case where there is only one detector element. An alternative would be to have a fan beam projections such as those shown in Figure 2.6. One can now use a point source of radiation to give a fan-shaped beam. On the other side of the object, a bank of detectors can be used to make all measurements in one fan simultaneously. Also, there is an added advantage

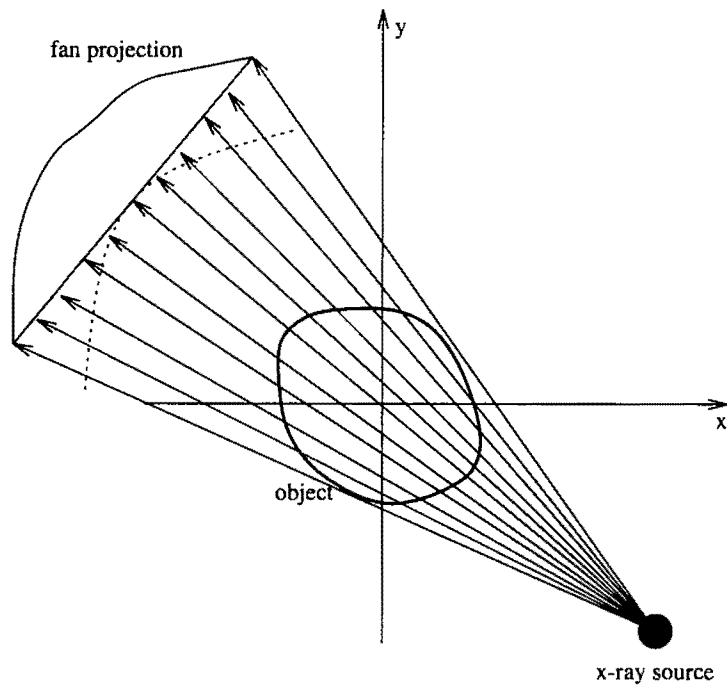


Figure 2.6: Fan beam projection

of magnified projections incident on the detector plane resulting in higher resolution. The object can then be rotated to get the desired number of projections. The detector elements can either be arranged in straight line or along an arc as shown by the dotted line. The backprojection algorithm has to be tailored for this configuration [2] as is described in the following section.

Fan Beam Filtered Backprojection

We now derive the backprojection algorithm for reconstruction with fan projections on a detector plane consisting of equispaced collinear elements. In terms of parallel projection data $P_\theta(t)$, the reconstructed image is given by equation 2.20

which can be rewritten as follows

$$f(x, y) = \frac{1}{2} \int_0^{2\pi} \int_{-t_m}^{t_m} P_\theta(t) h(x \cos \theta + y \sin \theta - t) dt d\theta \quad (2.31)$$

where t_m is the value of t for which $P_\theta(t) = 0$ with $|t| > t_m$ in all projections. We rewrite this equation in polar coordinates (r, ϕ) for ease of derivation.

$$x = r \cos \phi \quad y = r \sin \phi \quad (2.32)$$

$$f(x, y) = \frac{1}{2} \int_0^{2\pi} \int_{-t_m}^{t_m} P_\theta(t) h(x \cos \theta + y \sin \theta - t) dt d\theta \quad (2.33)$$

we get

$$f(r, \phi) = \frac{1}{2} \int_0^{2\pi} \int_{-t_m}^{t_m} P_\theta(t) h(r \cos(\theta - \phi) - t) dt d\theta \quad (2.34)$$

For parallel beam case, variables θ and t as shown in Figure 2.1 were sufficient to represent the projection data. When we move on to fan beam case, we need to introduce new variables β and γ as shown in Figure 2.7. Let the fan beam projections be denoted by $R_\beta(s)$. In the following discussion, we will start with the parallel beam case as given by equation 2.34 and introduce the new variables β and γ , and derive the corresponding fan beam backprojection algorithm.

Now referring to Figure 2.7, although the projections are measured along the line $D_1 D_2$, for theoretical purposes, we assume the existence of an imaginary detector line $D'_1 D'_2$ passing through the origin. Figure 2.8 is a zoomed version of Figure 2.7. In both the figures, the ray integral along SB can be associated with point A on $D'_1 D'_2$ as opposed to point B on $D_1 D_2$. Also, the fan projection $R_\beta(s)$ can be associated with imaginary detector line $D'_1 D'_2$.

Referring to Figure 2.8, if parallel projection data were generated for the object under consideration, the ray SA would belong to a parallel projection $P_\theta(t)$ with θ

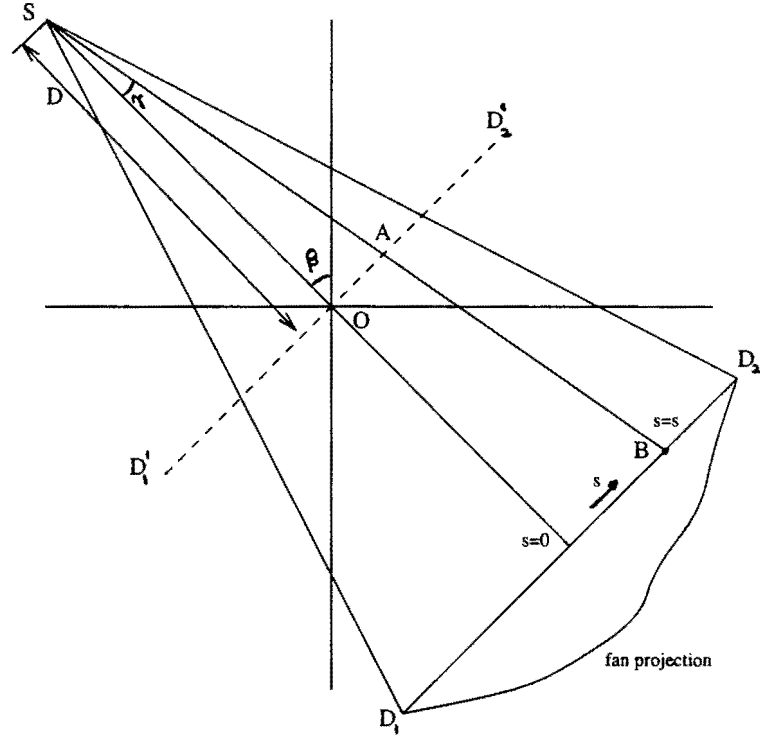


Figure 2.7: Projection parameters for equispaced collinear detectors

and t as shown. One can then write the following relationships

$$\begin{aligned}
 t &= s \cos \gamma & \theta &= \beta + \gamma \\
 t &= \frac{sD}{\sqrt{D^2 + s^2}} & \theta &= \beta + \arctan \frac{s}{D} \\
 dt d\theta &= J ds d\beta
 \end{aligned} \tag{2.35}$$

where J is the jacobian given by

$$J = \frac{D^3}{(D^2 + s^2)^{3/2}} \tag{2.36}$$

Using this, equation 2.34 can be expressed as

$$f(r, \phi) = \frac{1}{2} \int_{\eta_m}^{2\pi - \eta_m} \int_{-s_m}^{s_m} P_{\beta + \gamma}(\lambda) \cdot h[r \cos(\beta + \eta - \phi) - \lambda] \cdot J ds d\beta \tag{2.37}$$

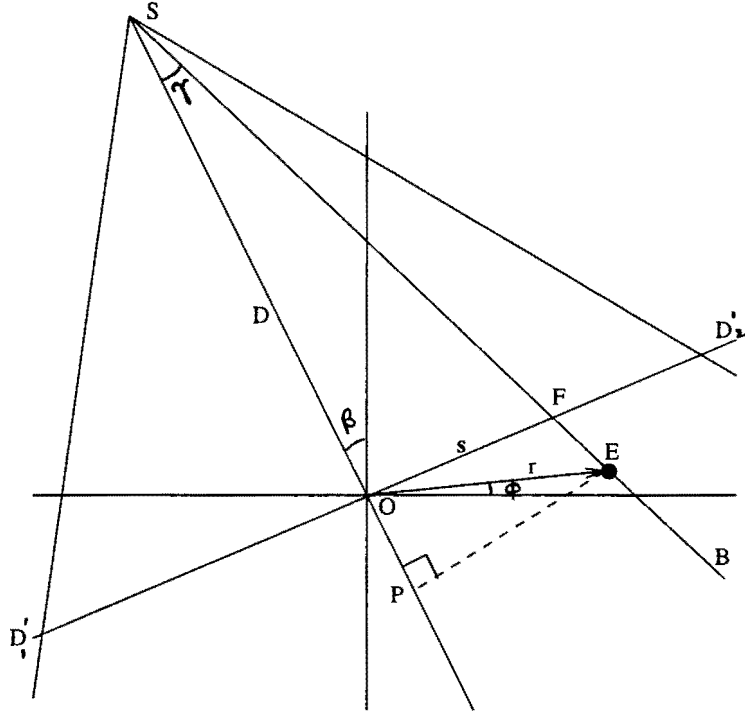


Figure 2.9: Parameters used for calculation of U and s'

as

$$f(r, \phi) = \frac{1}{2} \int_0^{2\pi} \int_{-s_m}^{s_m} R_\beta(s) h(r \cos(\beta + \eta - \phi) - \lambda) \cdot J ds d\beta \quad (2.39)$$

In order to express this formula in a filtered backprojection form, the argument of h is manipulated as follows

$$\begin{aligned} & r \cos(\beta + \eta - \phi) - \lambda \\ &= r \cos(\beta - \phi) \frac{Ds}{\sqrt{D^2 + s^2}} - (D + r \sin(\beta - \phi)) \frac{s}{\sqrt{D^2 + s^2}} \end{aligned} \quad (2.40)$$

A new variable U is now defined for every pixel in polar coordinates (r, ϕ) as the ratio of the distance SP (Figure 2.9), which is the projection of the source to pixel line SE on the central ray to the source-to-center distance.

$$U(r, \phi, \beta) = \frac{\overline{SO} + \overline{OP}}{D}$$

$$= \frac{D + r \sin(\beta - \theta)}{D} \quad (2.41)$$

Also, let s' denote the value of s for the ray passing through (r, ϕ) . That would be the distance \overline{OF} . Therefore, we have

$$\begin{aligned} \frac{s'}{\overline{SO}} &= \frac{\overline{EP}}{\overline{SP}} \\ s' &= D \frac{r \cos(\beta - \phi)}{D + r \sin(\beta - \phi)} \end{aligned} \quad (2.42)$$

Equations 2.41 and 2.42 can be used to express 2.40 in terms of U and s' as

$$r \cos(\beta + \eta - \phi) - \lambda = \frac{s'UD}{\sqrt{D^2 + s'^2}} - \frac{sUD}{\sqrt{D^2 + s^2}} \quad (2.43)$$

Substituting this in 2.39, we get

$$f(r, \phi) = \frac{1}{2} \int_0^{2\pi} \int_{-s_m}^{s_m} R_\beta(s) h \left[(s' - s) \frac{UD}{\sqrt{D^2 + s^2}} \right] J ds d\beta \quad (2.44)$$

Comparing this with 2.19, we can write

$$h \left[(s' - s) \frac{UD}{\sqrt{D^2 + s^2}} \right] = \int_{-\infty}^{\infty} |\omega| e^{j2\pi\omega(s'-s)\left(\frac{UD}{\sqrt{D^2+s^2}}\right)} d\omega \quad (2.45)$$

Using the transformation

$$\begin{aligned} \omega' &= \omega \frac{UD}{\sqrt{D^2 + s^2}} \\ d\omega' &= d\omega \frac{UD}{\sqrt{D^2 + s^2}} \end{aligned} \quad (2.46)$$

we can rewrite 2.45 as follows:

$$\begin{aligned} h \left[(s' - s) \frac{UD}{\sqrt{D^2 + s^2}} \right] &= \frac{D^2 + s^2}{U^2 D^2} \int_{-\infty}^{\infty} |\omega'| e^{j2\pi(s'-s)\omega'} d\omega' \\ &= \frac{D^2 + s^2}{U^2 D^2} h(s' - s) \end{aligned} \quad (2.47)$$

Substituting this in 2.44 we get

$$f(r, \phi) = \frac{1}{2} \int_0^{2\pi} \frac{1}{U^2} \int_{-s_m}^{s_m} R_\beta(s) g(s' - s) \frac{D}{\sqrt{D^2 + s^2}} ds d\beta \quad (2.48)$$

where

$$g(s) = \frac{1}{2} h(s) \quad (2.49)$$

Displaced Center-of-rotation

The reconstruction algorithm above is derived based on the assumption that the mathematical center-of-rotation is collinear with the midline of the fan beam. In practice a constant misalignment can occur when the x-ray source, the sample or the detector array is mispositioned. Consider the fan beam geometry depicted in Figure 2.10 in which the midline is displaced from the center-of-rotation by a constant value τ for every angle β . Now exactly the same steps as in equation 2.35 to 2.48 are repeated taking τ into account as follows [3]

$$\begin{aligned} t &= (s + \tau) \cos \gamma & \theta &= \beta + \gamma \\ t &= \frac{(s + \tau)D}{\sqrt{D^2 + s^2}} & \theta &= \beta + \arctan \frac{s}{D} \\ dt d\theta &= J ds d\beta \\ \text{where } J &= \frac{(D^2 - \tau s)D}{(D^2 + s^2)^{3/2}} \end{aligned} \quad (2.50)$$

This results in

$$f(r, \phi) = \frac{1}{2} \int_0^{2\pi} \int_{-s_m}^{s_m} R_\beta(s) h(r \cos(\beta + \eta - \phi) - \lambda) \cdot J ds d\beta \quad (2.51)$$

where

$$\lambda = \frac{D(s + \tau)}{\sqrt{D^2 + s^2}} \quad (2.52)$$

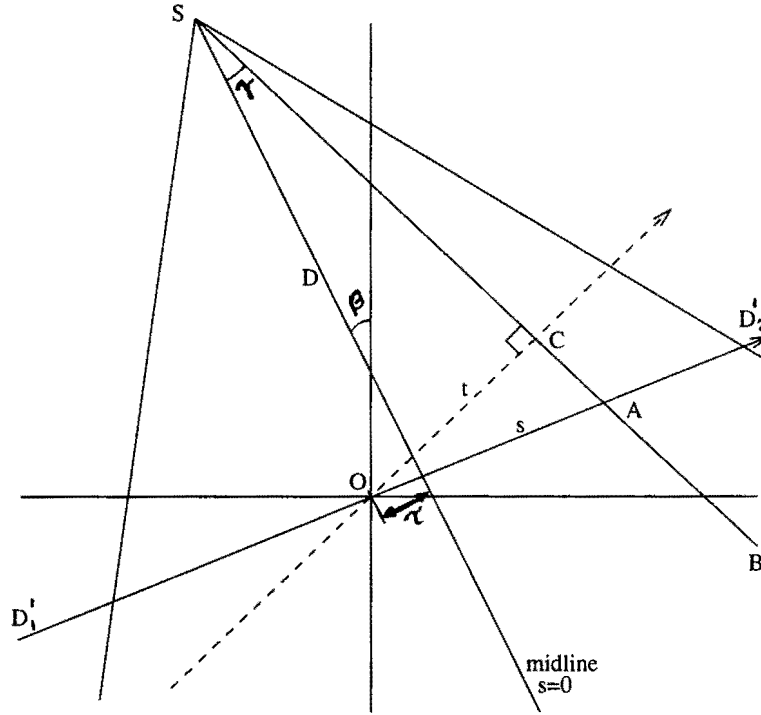


Figure 2.10: Fan beam geometry with displaced center-of-rotation

The argument of the filter h can be written as

$$r \cos(\beta + \eta - \phi) - \lambda = \frac{s'UD}{\sqrt{D^2 + s^2}} - \frac{sUD}{\sqrt{D^2 + s^2}} \quad (2.53)$$

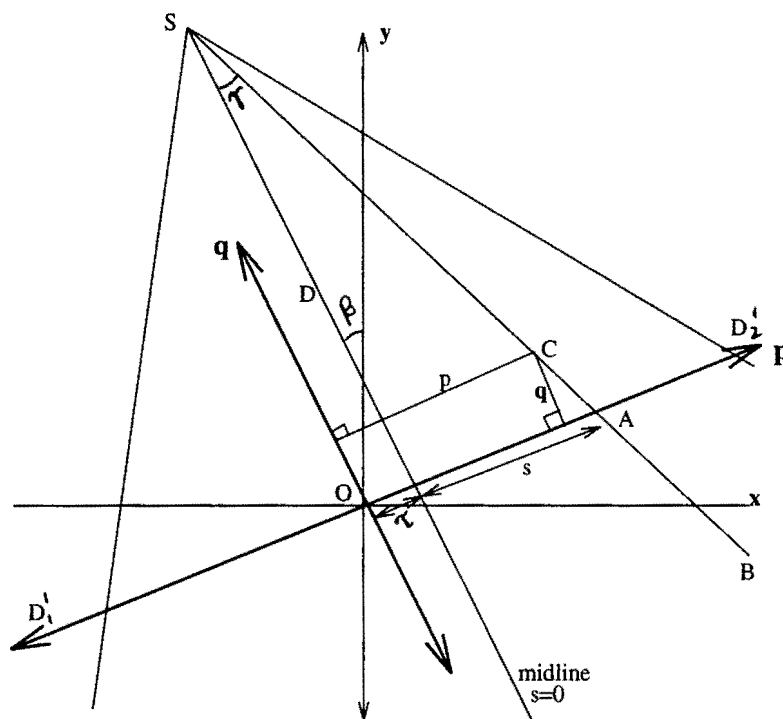
where

$$U(r, \phi, \beta) = \frac{D + r \sin(\beta - \theta)}{D} \quad (2.54)$$

$$s' = D \frac{r \cos(\beta - \phi) - \tau}{D + r \sin(\beta - \phi)} \quad (2.55)$$

This results in

$$f(r, \phi) = \frac{1}{2} \int_0^{2\pi} \frac{1}{U^2} \int_{-s_m}^{s_m} R_\beta(s) g(s' - s) \frac{D^2 - \tau s}{D \sqrt{D^2 + s^2}} ds d\beta \quad (2.56)$$

Figure 2.11: Rotated coordinate system (p, q)

Simplification

The expression in 2.56 can be further simplified as by replacing the (r, ϕ) coordinate system by rotated (p, q) system as shown in Figure 2.11. The location of a point (p, q) is given by

$$\begin{aligned} p &= x \cos \beta + y \sin \beta \\ q &= -x \sin \beta + y \cos \beta \end{aligned} \quad (2.57)$$

Using these coordinates, we can write the expressions for U and s' as

$$s' = \frac{Dp}{D - q} - \tau \quad (2.58)$$

$$U(x, y, \beta) = \frac{D - q}{D} \quad (2.59)$$

The fan beam reconstruction given by equation 2.56 can then be rewritten as follows for ease of understanding

$$f(p, q) = \frac{1}{2} \int_0^{2\pi} \frac{1}{U^2} Q_\beta(s') d\beta \quad (2.60)$$

where

$$Q_\beta(s) = R'_\beta(s) * g(s) \quad (2.61)$$

and

$$R'_\beta(s) = R_\beta(s) \cdot \frac{D^2 - \tau s}{D\sqrt{D^2 + s^2}} \quad (2.62)$$

and U and s' are given by equations 2.58 and 2.59 respectively.

Cone Beam Filtered Backprojection

The image intensifier outputs a two dimensional projection of the object. One slice of this projection is used to reconstruct a two dimensional slice of the object as shown in Figure 2.12. The entire object can be reconstructed by taking a series of two dimensional reconstructions and stacking them together. This would however be very time consuming. Instead, each of the slices in the projection can be backprojected along their corresponding fan. Each slice is considered separately and their contributions to the 3D-object are added up to give 3D-backprojection.

To derive the reconstruction algorithm, we first rewrite the equation 2.60 as follows

$$f(p, q) = \frac{1}{2} \int_0^{2\pi} \frac{D^2}{(D-p)^2} \int_{-s_m}^{s_m} R_\beta(s) g\left(\frac{Dp}{D-q} - s\right) \frac{D^2 - \tau s}{D\sqrt{D^2 + s^2}} ds d\beta \quad (2.63)$$

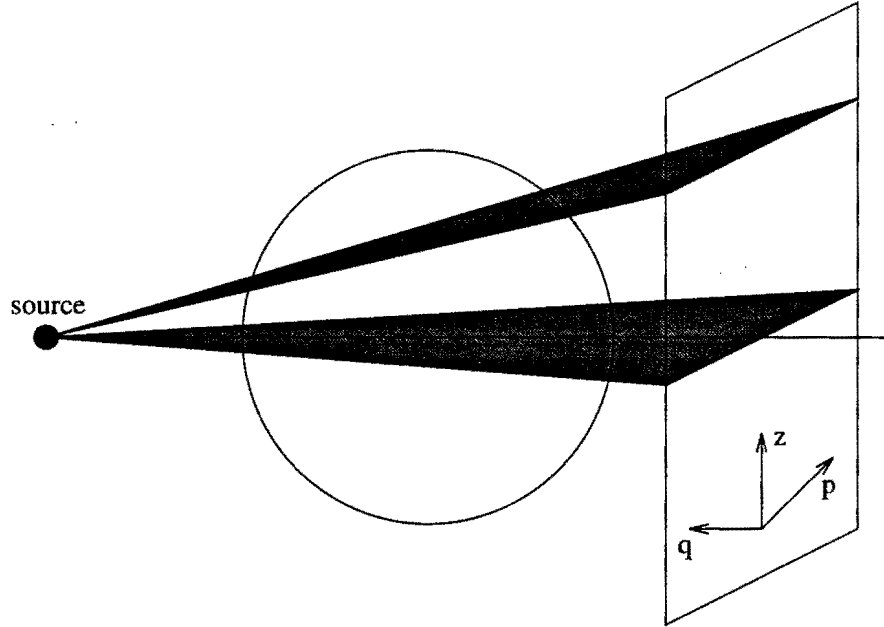


Figure 2.12: Cone beam reconstruction from tilted fans

As the fan is tilted out of the plane of rotation, the coordinate system of the reconstructed point change. Let (\tilde{p}, \tilde{q}) represent the new coordinate system as shown in Figure 2.13. Also let \tilde{z} represent the height of the fan above the plane of rotation. The distance D and angular differential β also change and can be given by \tilde{D} and $\tilde{\beta}$ where

$$\tilde{D}^2 = D^2 + \tilde{z}^2 \quad (2.64)$$

$$d\tilde{\beta} \cdot \tilde{D} = D \cdot d\beta \quad (2.65)$$

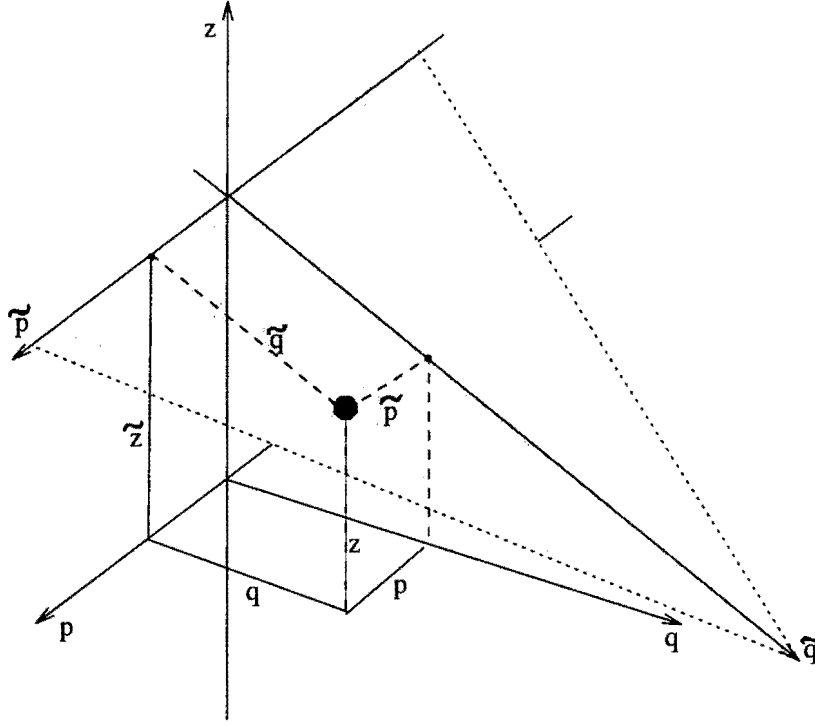


Figure 2.13: Coordinate system for tilted fan

Substituting these new variables in equation 2.64 and writing the projection as $R_{\tilde{\beta}}(p, \tilde{z})$, we get

$$f(\tilde{p}, \tilde{q}) = \frac{1}{2} \int_0^{2\pi} \frac{\tilde{D}^2}{\tilde{D} - \tilde{p}}^2 \int_{-s_m}^{s_m} R_{\tilde{\beta}}(s, \tilde{z}) g\left(\frac{\tilde{D}\tilde{p}}{(\tilde{D} - \tilde{q})^2}\right) \frac{\tilde{D}^2 - \tau s}{\tilde{D}\sqrt{\tilde{D}^2 + s^2}} ds d\tilde{\beta} \quad (2.66)$$

By substituting

$$\begin{aligned} \tilde{p} &= p \\ \frac{\tilde{q}}{\tilde{D}} &= \frac{q}{D} \end{aligned} \quad (2.67)$$

$$\frac{\tilde{z}}{D} = \frac{z}{D - q}$$

we obtain

$$f(p, q, z) = \frac{1}{2} \int_0^{2\pi} \frac{D^2}{(D - p)^2} \cdot \int_{-s_m}^{s_m} R_\beta(s, \tilde{z}) g \left(\frac{Dp}{D - q} - s \right) \frac{D^2 - \tau s}{D \sqrt{D^2 + s^2 + \tilde{z}^2}} ds d\beta \quad (2.68)$$

Three dimensional cone beam reconstruction can then be written as follows for ease of understanding

$$f(p, q, z) = \frac{1}{2} \int_0^{2\pi} \frac{1}{U^2} Q_\beta(s', \tilde{z}) d\beta \quad (2.69)$$

$$\text{where } Q_\beta(s, \tilde{z}) = R'_\beta(s, \tilde{z}) * g(s) \quad (2.70)$$

$$R'_\beta(s, \tilde{z}) = R_\beta(s, \tilde{z}) \cdot \frac{D^2 - \tau s}{D \sqrt{D^2 + s^2 + \tilde{z}^2}} \quad (2.71)$$

$$U = \frac{D}{D - q} \quad (2.72)$$

$$s' = \frac{Dp}{D - q} - \tau \quad (2.73)$$

$$\tilde{z} = \frac{Dz}{D - q} \quad (2.74)$$

There is also an entirely different approach of tomographic reconstruction where we assume the cross sectional image to be an array of unknowns and then setting up algebraic equations for unknowns in terms of measured projection data [9]. However, this method lacks the accuracy and the speed of implementation. This method is used in situations where very sparse or limited angle data is available. There are several iterative reconstruction schemes [9] which can be used as postprocessing steps after the initial reconstruction.

CHAPTER 3. SETUP

This chapter describes the real time radiography setup on which tomographic inspection capability is developed. Figure 3 shows a block diagram of the various components of the system. This setup is typical of a real-time x-ray inspection facility. The dotted box encloses the equipment in the radiation sealed vault. X-rays from the generator are intercepted by the sample placed on 5-axis positioner and fall on the face plate of the image intensifier. Image intensifier converts the incident photon flux into visual image which is captured by the camera. The video signal thus generated is digitized using a frame grabber. The personal computer acts as an overall controller. Generator, positioners and frame grabber are controlled by the PC. The Digital Signal Processing (DSP) board can be used for fast data processing. The network connection on the PC allows for remote and/or distributed reconstruction process.

Generator

There are two different generators used: IXRS320/1600A[15] and FXE-200.50[16]. The IXRS320/3200, manufactured by IRT corporation ranges from 20 to 320 kilovolt and has a power rating of 3200 Watts. The focal spot size varies from 0.8-1.8 mm. The FXE-200.50 is manufactured by FeinFocus and uses microfocus x-ray technology.

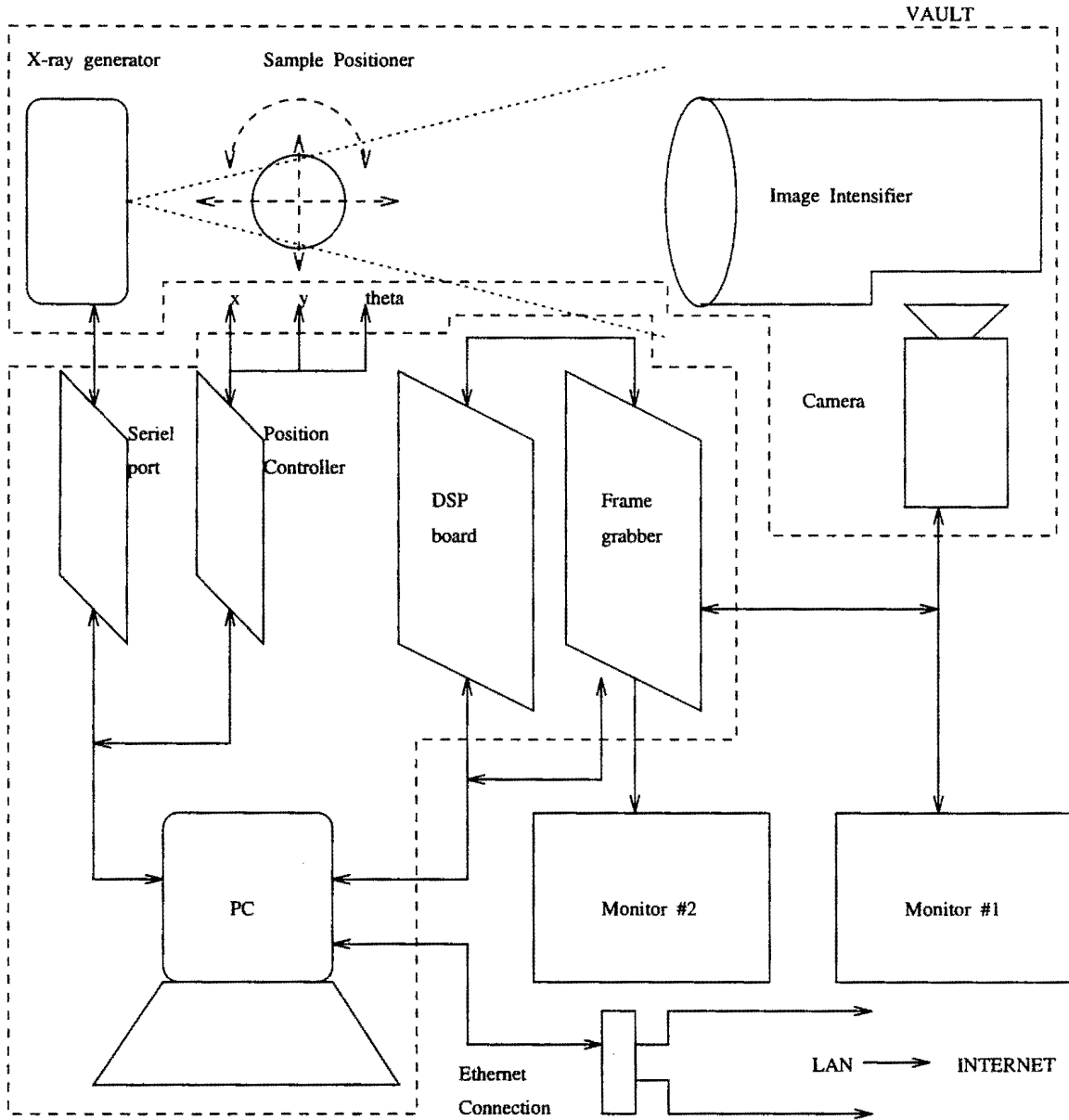


Figure 3.1: System setup

The focal spot size can be adjustable with the range of 0.005-1 mm. However, the voltage and power rating is limited to 200KV and 160 Watt respectively. The extent of focal spot at the source of X-ray radiation determines the geometrical resolution of the projected radiograph. Smaller focal spot size requires a reduction of the electron beam power which in turn limits the maximum output photon flux.

Both the generators can be operated under remote control by the host PC. The x-ray controller and the host computer are connected to each other via a serial RS 232C interface. Communication occurs according to the specified protocols.

Positioning Control

The sample positioner has 5-axis of movement. These axes are driven by individual Parker Compumotor steppers. The motor drives use a microstep mode which allows for resolution as high as 100,000 steps/inch and 10,000 steps/degree. Microstepping is achieved by subdividing the basic motor step by proportioning the current in the two stator windings [18]. In this way step size is reduced and low speed smoothness is dramatically improved.

Microprocessor based I/O mapped indexer cards, namely PC23 made by Compumotor are used to control the axes. The card connects to a separate adapter box (MC5300 motor controller) to provide an interface to the external motor drivers and limit switches. Figure 3.2 illustrates this configuration. Positioning control is achieved by communicating with the PC23 card in the specified command language [17].

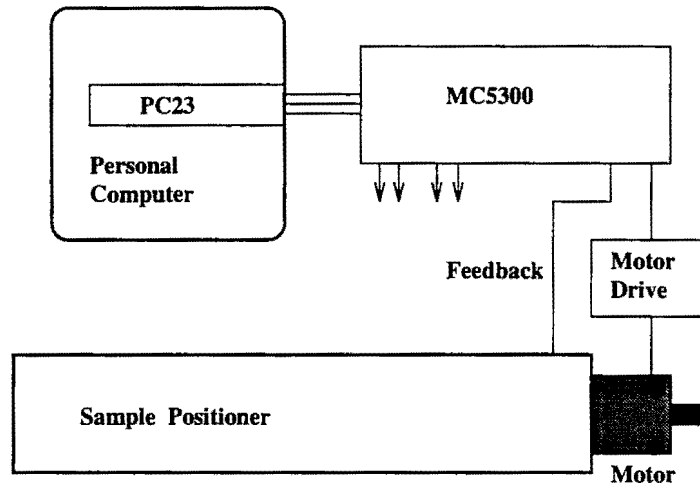


Figure 3.2: Motion control

Image Intensifier

The Image Intensifier (II) is used as the detector for the X-rays. It converts the incident X-ray photon flux to an optical image. Figure 3.3 shows the basic construction of the II tube. The input scintillator screen made up of phosphorescent material acts as the primary detecting element. It consists of a phosphorescent material which converts the X-ray photons to optical photons. However, the conversion efficiency is as low as 1%. Therefore, the optical photons are used to generate electrons using a photocathode. These electrons are then accelerated and focused onto a output conversion phosphor screen that is about 10 times smaller in diameter than the input conversion screen. The high energy electrons coupled with minification process

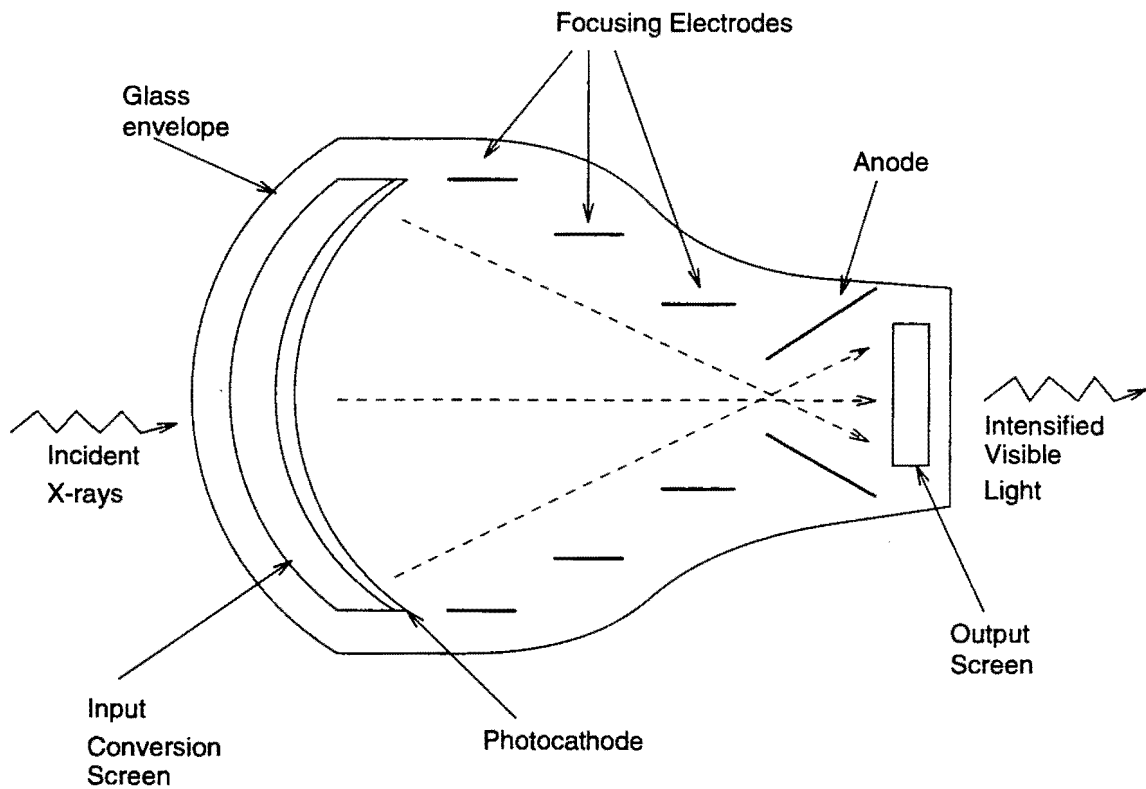


Figure 3.3: Image intensifier

results in intensified visible light from the output phosphor [12].

Camera

The camera captures the image at the output phosphor of II and converts it into a standard video signal. The cameras used have an 512x512 CCD element array. The size of this CCD array and the area of the output phosphor in the field of view and the phosphor blooming [12] determine the spatial resolution. The camera should be well focussed to prevent any optical blurring.

Frame Grabber

The video signal from the camera is digitized for further processing. The Data Translation's DT2867 is used as the 8 bit frame grabber [20]. It is a single IBM PC AT plug-in board. It has software selectable input gain, offset, and range to accommodate low-light or low quality video signals with full resolution. There is built in 25 MHz 16-bit processing hardware consisting of three arithmetic logic units and three multipliers. The board memory consists of two 8-bit frame buffers and one 16-bit frame buffer.

I/O mapped board registers are used to program the board. All functions of DT2867 are controlled by writing commands to the registers using standard 16-bit I/O instructions. A detailed register summary can be found in [20].

DSP Board

The DSP board can be used for accelerated processing of the input data. Eighteen Eight Laboratories PL2510 processor - a floating point array processor, built on a single full length PC board is used [21]. It contains a microcoded fundamental library burned into a EPROM optimized for performing logical and mathematical operations on vectors, arrays, matrices, tables and lists of data. These routines can be linked into the host control program on the PC.

Network Connection

The PC is connected to the LAN by a standard ethernet card. Socket interface to the internet can be obtained by any socket library such as Microsoft's *winsock*

under MS-Windows 3.1 which is used here. This allows for remote implementation of the reconstruction algorithm, such as on a more powerful UNIX workstation. The network interface becomes imperative for three dimensional reconstruction, where the projections are too large to be stored out and have to be processed on the fly with data acquisition. Three dimensional reconstruction algorithm must be implemented on powerful UNIX workstations because of the large amount of memory required. The implementation on the PC would be extremely slow. The network also opens up the power of distributed reconstruction if several computers are connected over the LAN.

CHAPTER 4. IMPLEMENTATION

This chapter deals with the various issues concerning implementation of tomographic reconstruction. The chapter begins with description of data acquisition. Then, we step through the algorithm followed by discussion on improving the system performance. Finally, cone beam three dimensional reconstruction is discussed.

Data Acquisition

X-ray Physics

The interaction of x-rays with homogeneous isotropic material is given by (Figure 4.1(a))

$$I = I_0 e^{-\mu x} \quad (4.1)$$

where I_0 is the incident beam intensity

I is the transmitted beam intensity

μ is the linear absorption coefficient of the material

and x is the distance traversed by the x-rays in the material

(4.2)

For a two-dimensional case, we can rewrite this equation as

$$I = I_0 e^{-\int_{ray} \mu(x,y) ds} \quad (4.3)$$

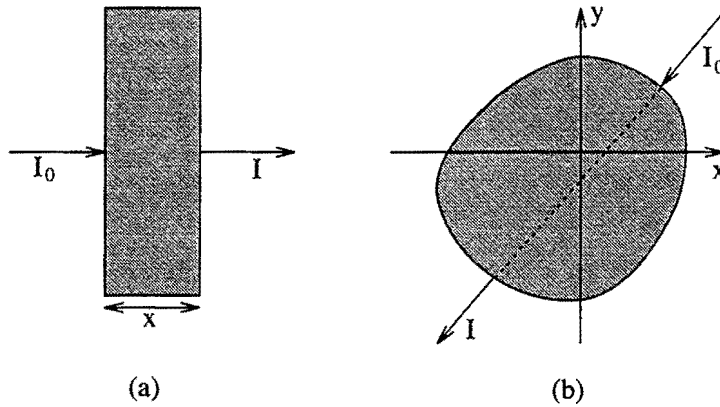


Figure 4.1: Lambert's Law (a) One dimensional case (b) Two dimensional case

or

$$\int_{ray} \mu(x, y) ds = \ln \left(\frac{I_0}{I} \right) \quad (4.4)$$

The left hand side precisely constitutes a ray integral for the projection. This is shown in Figure 4.1(b). Therefore, we need to take the measure of incident I_0 and transmitted beam intensity I (which forms the measured data) and use it to calculate the projection integral using equation 4.4.

Acquiring Projection

There are number of detectors which can be used to determine the x-ray beam intensity. Traditionally, CT systems used scintillation type detector arrays which count photons. Examples of commonly used scintillation materials are Ge, NaI, etc. The advantage of using such detectors is very high dynamic range (proportional to time taken to acquire a sample) and the sensitivity to x-ray energy which enables the object function $f(x, y)$ to be reconstructed in a narrow band of energy. This becomes an important issue because, in equation 4.4, $\mu(x, y)$ does depend on the x-ray

energy. However, the disadvantage is that to acquire data quickly, the cost of the detector array and the electronics involved becomes exorbitant. Most of the medical CT imaging is done using such arrays.

There are other types of detectors such as image intensifier and scintillation glasses which convert the incident x-ray flux into visible light. This is typically captured by the camera and digitized. The other option is to have a fiber optic bundle deliver this light to a photosensitive array and then digitize it. This system has the advantage of being economical and hence affordable for many industrial applications. The most apparent disadvantage is the loss of energy sensitivity which results in $f(x, y)$ integrated over the x-ray spectrum. The image intensifier is used most commonly in a real time inspection system and hence we will be used in all the discussion that follows.

Image intensifier output consists of a fluorescent image which is representative of I . This is converted by the camera into a video signal. DT2867 used as a frame grabber digitizes this signal with an 8-bit analog to digital (A/D) converter in real time i.e. at the rate of 30 frames/second. The digitized image is 640x480 pixels. Using equation 4.4 the projection data $R_{beta}(na)$ to be used for reconstruction is given by

$$R_{\beta}(na) = \ln \frac{G_0}{G_{\beta}(na)} \quad (4.5)$$

where G_0 is the gray scale level intensity without the sample

$G_{\beta}(na)$ is the slice of the digitized image at angle β

a is the the sampling interval

$$\text{and } 0 \leq n \leq 640 \quad (4.6)$$

The slice $G_\beta(na)$ read from the frame grabber consists of gray scales ranging from 0 to G_{max} where

$$G_{max} = 2^8 - 1 \quad (4.7)$$

The value of G_0 cannot be determined once the x-ray flux is high enough to saturate the image intensifier. Hence, we proceed by making the assumption

$$G_0 = G_{max} \quad (4.8)$$

Now from equation 4.6, $G_\beta(na) = 0$ at any point implies that $R_\beta(na) = \infty$ at that point. This suggests that for the line integral along the corresponding ray, either the material is infinitely thick ($x = \infty$) or has an infinite attenuation coefficient ($\mu = \infty$). The practical reason is that the gray scale intensity resulting due to that line integral is less than the minimum nonzero value which is 1. Therefore, we need to *clip the slice* to allow for minimum of $G(na) = 1$.

An aluminum cylinder with a 1.0 inch diameter and 3 holes drilled in it is used as a test sample as shown in Figure 4.2. The sample is rotated at different angles and the same slice taken to get the entire sinogram as shown in Figure 4.3. The maximum value in the projection will be

$$R_{\beta(max)} = \ln \left(\frac{G_{max}}{1} \right) \quad (4.9)$$

The normalized projection will be given by

$$R_\beta(na) = \frac{\ln \left(\frac{G_{max}}{G(na)} \right)}{\ln G_{max}} \quad (4.10)$$

Sampling Interval

To determine the sampling interval, which is distance between the individual sampling elements of the detector, we first need to calculate the dimensions of the

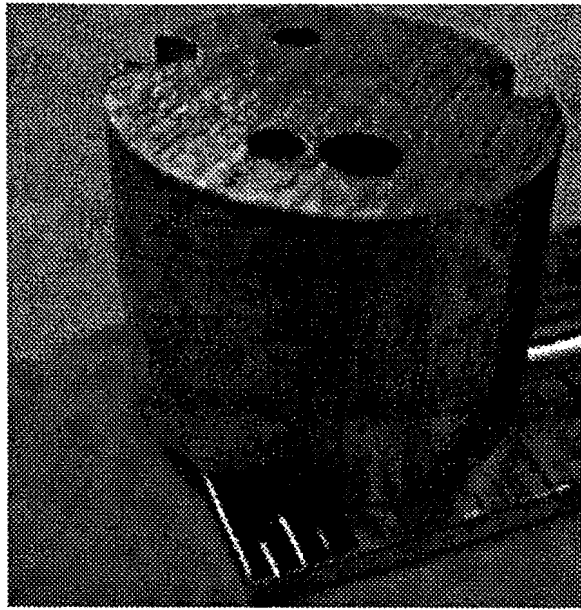


Figure 4.2: Test sample

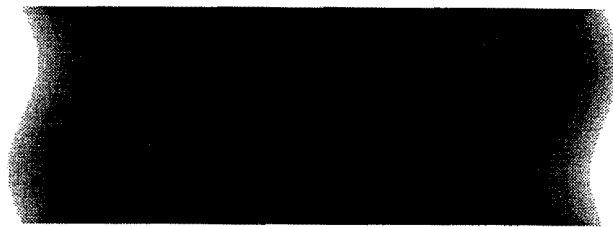


Figure 4.3: Sinogram

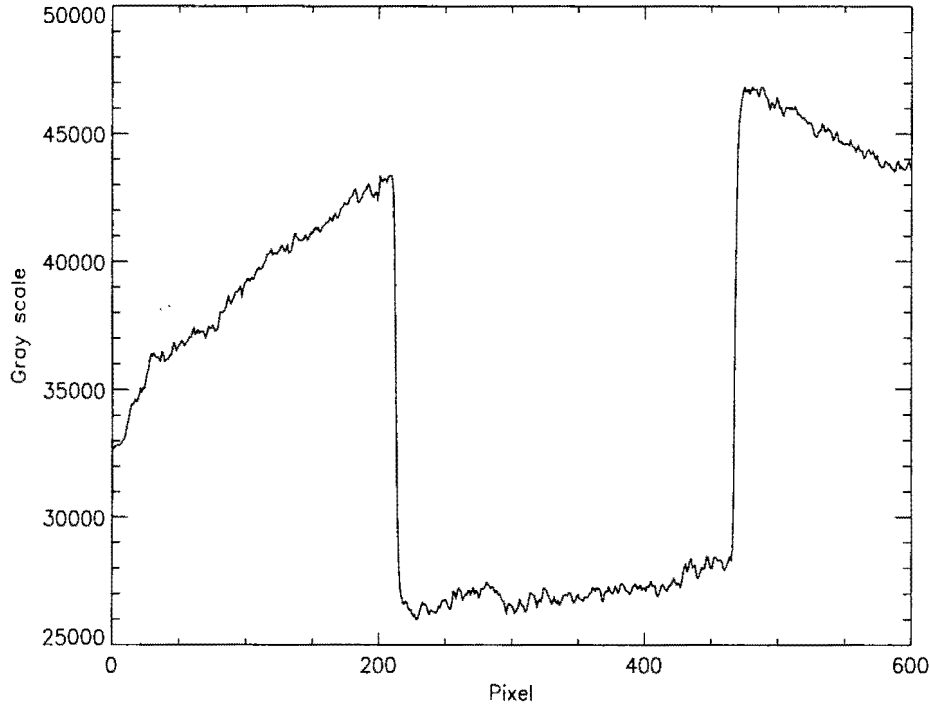


Figure 4.4: Slice for calculating the sampling interval a

image obtained from the camera. We can determine this by taking images of a regular shape such as a rectangular plate slapped on the face plate of image intensifier. The slice across the plate is as shown in the Figure 4.4. The number of pixels occupied by the plate dimension can be found. Then

$$A = \frac{\text{plate dimension in inches}}{\text{number of pixels}} \quad (4.11)$$

This can be repeated for several dimensions and averaged to remove any random errors. Factors which influence the sampling interval are:

1. Number of pixels in the field of view of image intensifier and
2. Area of the image formed by image intensifier which is captured by the camera.

Since, we are working with fan beam geometry, there is a magnification factor involved. Let DD and D be the source-sample and source-detector distances respectively. These are determined using a tape measure. Typically

$$DD \approx 60 \dots 80 \text{ inches}$$

$$D \approx 8 \dots 40 \text{ inches}$$

The magnification factor m

$$m = \frac{DD}{D} \approx 2 \dots 10 \quad (4.12)$$

This results in effective sampling interval a at the sample to be

$$a = \frac{A}{m} \quad (4.13)$$

Alignment

For the tomographic scan to be accurate, the axis of rotation of the object should be exactly perpendicular to the plane of the fan. Figure 4.5(a) illustrates the tilt in axis of rotation by an angle $\delta\theta$. This results in data being collected across the extent of a cone as shown in Figure 4.5(b). Therefore

$$d = V \tan(\delta\theta) \quad (4.14)$$

where V is the field of view

In other words, if we want to resolve structures of size d , then the misalignment should be less than

$$\delta\theta = \arctan \frac{d}{V} \quad (4.15)$$

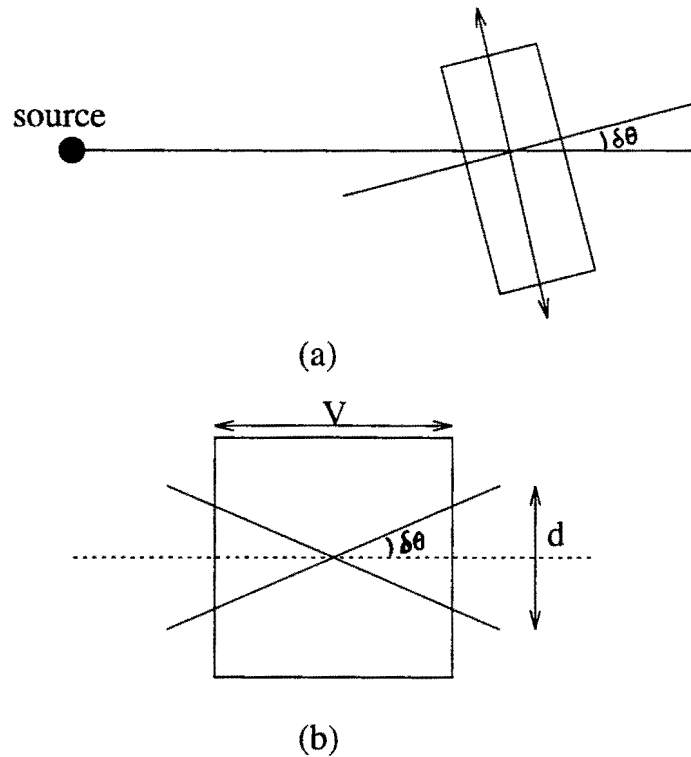


Figure 4.5: Misalignment

For example, if one wants to resolve 1mm structures with 25mm field of view, the misalignment should be less than 2.3° ; for 10μ structures with 3mm field of view, misalignment should be less than 0.19° .

The position controller used lacks one axis of freedom for accurately aligning the axis of rotation. The amount of misalignment can be observed and corrected by tracing the projection of the tip of a object such as a needle as it is rotated. The movement of the tip in the vertical direction is a measure of misalignment.

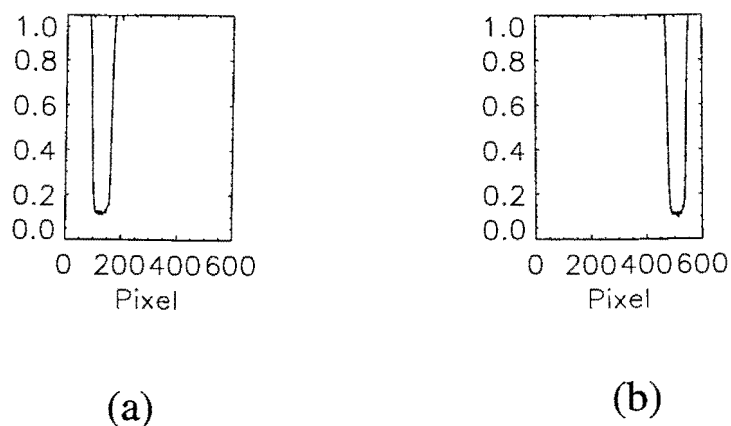


Figure 4.6: Projections for calculating center of rotation (a) Projection at 0° (b) Projection at 180°

Center of Rotation

The inspection setup is such that generator and the position controller are frequently moved around as the need arises. Therefore, it becomes necessary to calculate the center of rotation (COR) before starting a scan. Moreover, the knowledge of COR is needed by the reconstruction algorithm which executes on the fly after acquiring every projection.

To calculate the COR, two projections of an object at 0° and 180° are taken. Two such projections R_0 and R_{180} at 0° and 180° respectively are shown in Figure 4.6. The center of moment for these projection is found which is

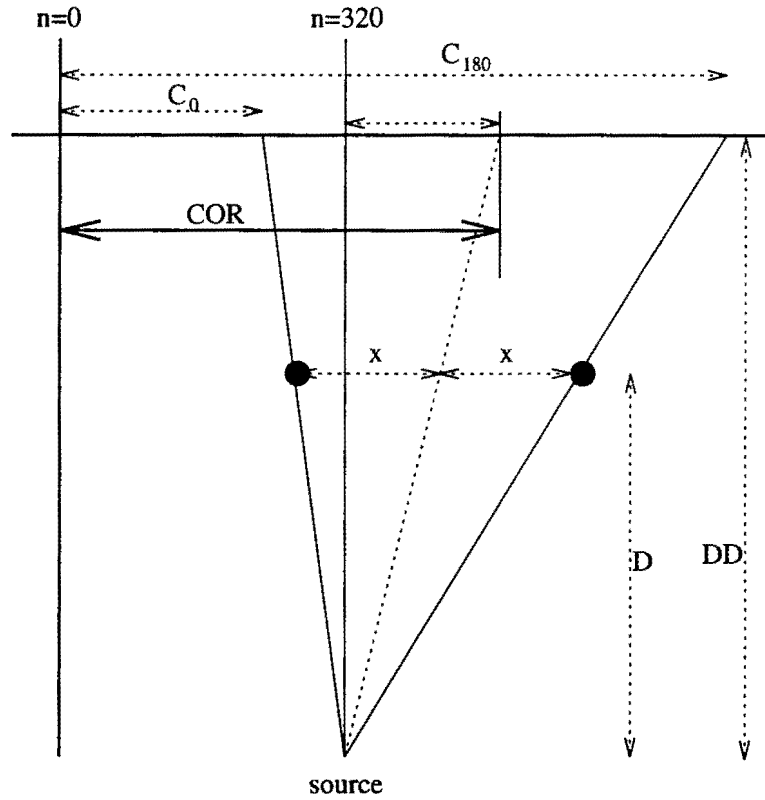


Figure 4.7: Center of rotation calculation

$$C = \frac{\sum_{n=0}^{n=640} (n \cdot R_{\beta}(na))}{640} \quad (4.16)$$

Let C_0 and C_{180} represent the center of moments of R_0 and R_{180} respectively as shown in Figure 4.7.

$$R_0 = \left(\frac{\tau}{m} - x \right) \cdot m$$

$$R_{180} = \left(\frac{\tau}{m} + x \right) \cdot m$$

Here m is the magnification and τ is the amount by which the COR is off from the center of projection which is 320. Now

$$R_0 + R_{180} = 2\tau \quad (4.17)$$

This gives us

$$\begin{aligned} COR &= \tau + 320 \\ &= \frac{(R_0 + R_{180})}{2} + 320 \end{aligned} \quad (4.18)$$

$$\text{and } \tau = (COR - 320) \quad (4.19)$$

Preferably the object used should have a radial symmetry and high attenuation to x-rays (such as allen wrench, needles, etc). However, for most of the cases, the projections from the object to be scanned itself can be used to calculate the COR. It should be realized that since we are using the center of moment to determine the geometric position of the object, the projections for COR determination should be saturated in the regions other than that occupied by the object. Otherwise, the background would cause a shift in the both the center of moments and hence the calculated COR would be incorrect.

Stepping through Fan Beam Reconstruction

In this section, we will single step through the application of filtered backprojection algorithm as outlined in the previous discussions. An aluminum cylinder with a 1.0 inch diameter and 3 holes drilled in it is used as a test sample. The relevant parameters used for reconstruction are as follows

DD = Source to detector distance = 68.0 inches

D = Source to sample distance = 15.0 inches

A = Size of individual detector elements = 0.0012 inches

N = Number of elements in one projection = 640 (NTSC width)

COR = Center of rotation = 322.43 pixels

K = Number of projections = 320

The various steps for computer implementation are as follows

Step 1:

The first step is to obtain projections $R_{\beta_i}(na)$ from each slice $G_{\beta_i}(na)$ using equation 4.10

$$R_{\beta}(na) = \frac{\ln \left(\frac{G_{max}}{G(na)} \right)}{\ln G_{max}} \quad (4.20)$$

where a is the sampling interval; n takes integer values such that $0 \leq n \leq 640$; β_i are the angles for which fan projections are known. One such slice and the its corresponding projection is shown in Figure 4.8(a) and Figure 4.8(b) respectively.

Step 2:

The next step is to generate for each fan projection $R_{\beta_i}(na)$ the corresponding modified projection $R'_{\beta_i}(na)$ given by equation 2.62

$$R'_{\beta_i}(na) = R_{\beta_i}(na) \cdot \frac{D^2 - \tau s}{D\sqrt{D^2 + s^2}} \quad (4.21)$$

where τ represents the displacement of the center-of-rotation from the midline given by equation 4.19. Figure 4.8(c) shows the modified projection.

Step 3:

The modified projection in Figure 4.8(c) has some high frequency components (noise) which will be greatly amplified after convolution with the

backprojection filter. Therefore, as suggested earlier by equation 2.24, some amount of smoothing is applied to reduce the high frequency noise. Hamming window is chosen as the smoothing function. It is given by

$$k[n] = \begin{cases} \zeta - \xi \cos(2\pi n/M), & 0 \leq n \leq M \\ 0, & \text{otherwise} \end{cases}$$

where $\zeta = 0.54$ and $\xi = 0.46$ (4.22)

M is the size of the window and is chosen to be 10 (We will discuss more about choosing the window size later). Figure 4.9(a) shows this filter in discrete-time domain. The corresponding frequency domain response is shown in Figure 4.10(a). Figure 4.8(d) shows the smoothed projection. The convolution is done using the technique described in [13]. The projection sequences are 640 elements in size. To prevent any aliasing during implementation of circular convolution, we have to choose the sequence length of at least $640 \times 2 = 1280$. For ease of FFT implementation, we choose the size which is power of two. This turns out to be $2^{11} = 2048$. Therefore, in Figure 4.10, the frequency is given by

$$\omega = \frac{2\pi}{2048} \cdot n \quad (4.23)$$

The dc component correspond to $n = 0$ and highest frequency corresponds to $n = 1024$.

Step 4:

Convolve each modified smoothed projection $R'_{\beta_i}(na)$ with $g(na)$ to generate the corresponding filtered projection

$$Q'_{\beta_i}(na) = R_{\beta_i}(na) * g(na) \quad (4.24)$$

The sequence $g(na)$ is given by

$$g(na) = \frac{1}{2}h(na) \quad (4.25)$$

where $h(na)$ is given by equation 2.30. Therefore

$$g(na) = \begin{cases} \frac{1}{8a^2}, & n = 0 \\ 0, & n \text{ even} \\ -\frac{1}{2n^2\pi^2a^2}, & n \text{ odd} \end{cases} \quad (4.26)$$

Figures 4.9(b) and 4.10(b) show this filter in discrete-time domain and frequency domain respectively.

Step 5:

Perform weighted backprojection of each filtered projection along the corresponding fan as given by equation 2.60. The sum of all backprojections is the reconstructed image

$$f(x, y) = \frac{2\pi}{K} \sum_{i=1}^K \frac{1}{U^2(x, y, \beta_i)} Q_{\beta_i}(s') \quad (4.27)$$

where K angles θ_i are those for which fan projections are known. For each angle θ_i , the transformed coordinates (p, q) are calculated for every pixel in the image plane using equation 2.5. These are used to calculate U and s' as given by equations 2.58 and 2.59. Now, using s' , we need to find out the element n' of $Q_{\beta_i}(na)$ corresponding to each pixel. s' is the actual distance measured in image plane. If the image is of size $L \times L$, L corresponds to same distance as 640 corresponds to in the filtered projection $Q_{\beta_i}(na)$. Therefore

$$n' = s' \cdot \frac{640}{L} \quad (4.28)$$

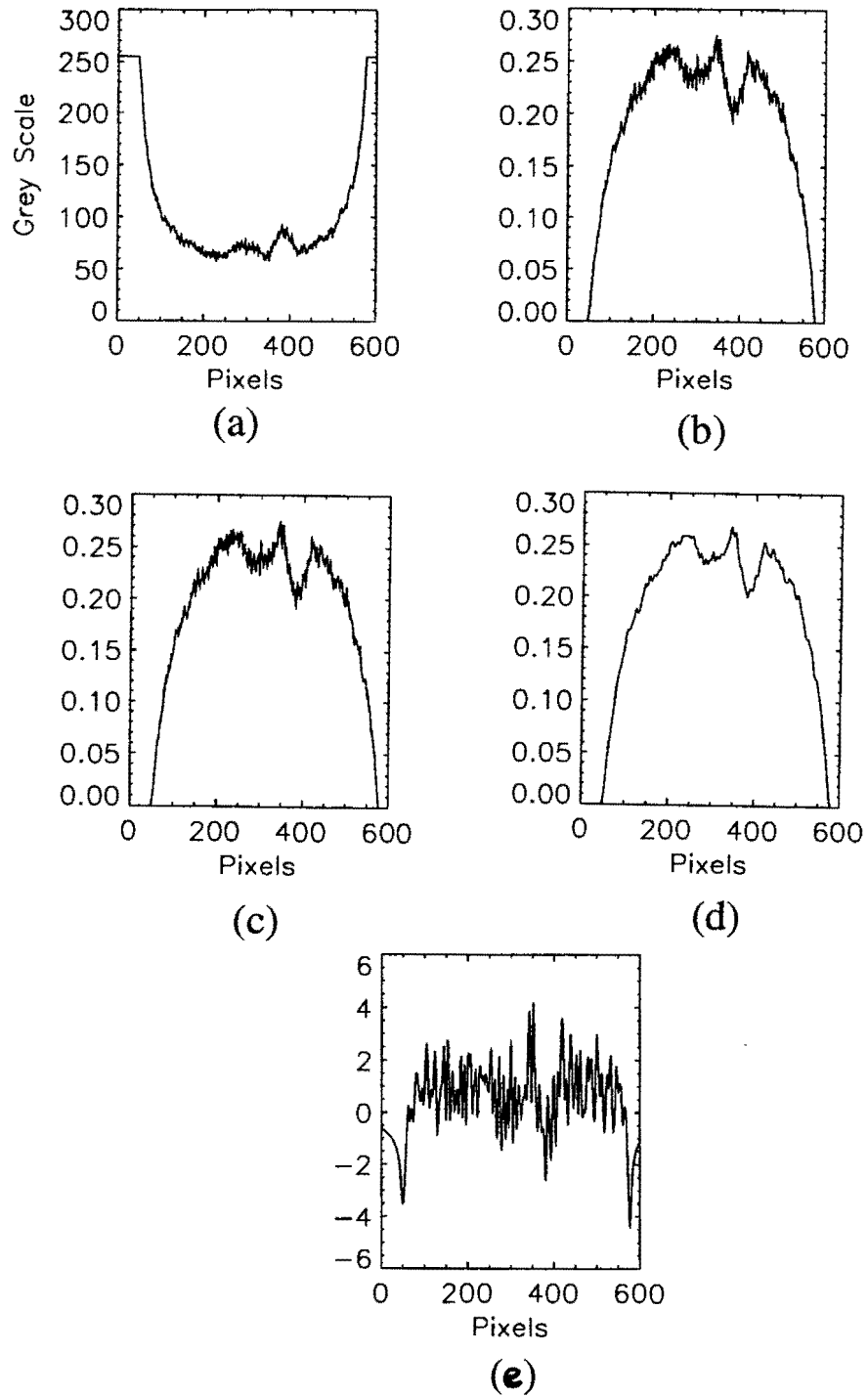


Figure 4.8: Reconstruction steps (a) Slice (b) Projection (c) Weighted projection (d) Smoothed projection (e) Filtered projection

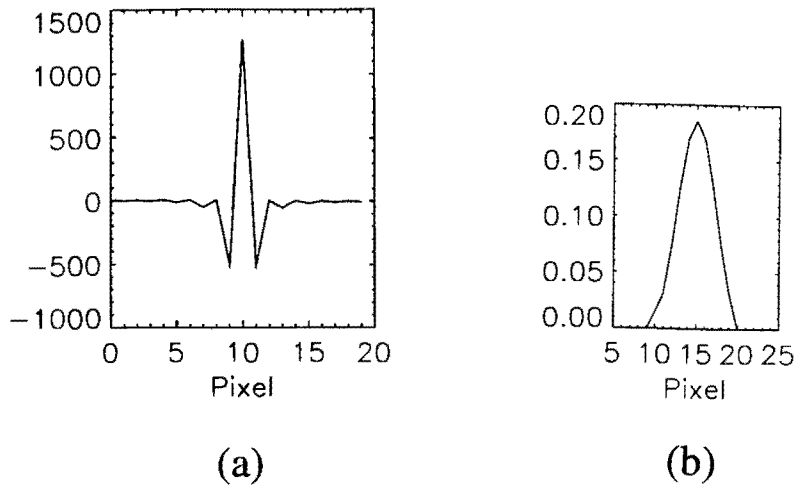


Figure 4.9: Time Domain (a) Backprojection kernel (b) Hamming window

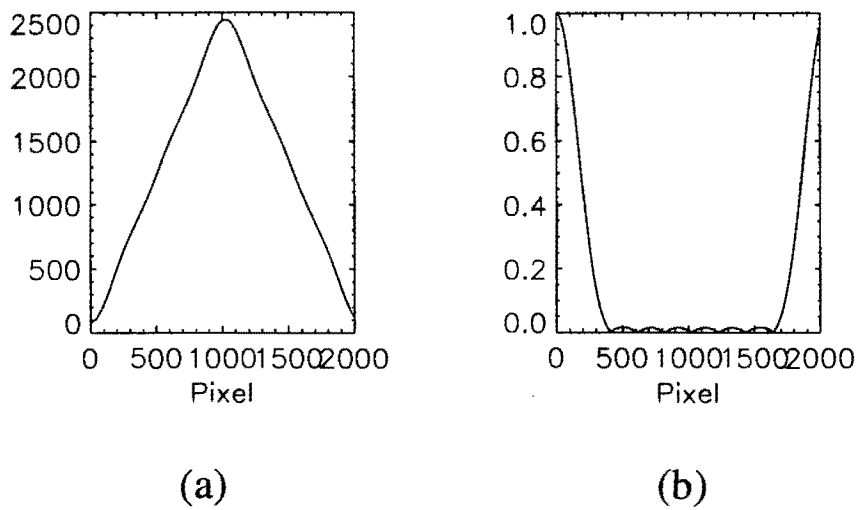


Figure 4.10: Frequency response (a) Backprojection kernel (b) Hamming window

The value of n' may not be an integer, in which case we choose the closest integer value. Also, if n' is greater than 640 or less than zero, there is no contribution to that pixel element from Q_{β_i} . Thus for each pixel, we add the contribution $\frac{1}{U^2}Q_{\beta_i}(n')$. The image after one such backprojection is shown in Figure 4.11(a). The final image after backprojecting entire sinogram is shown in Figure 4.11(b).

Cone Beam 3D Reconstruction

The implementation of 3D reconstruction is a straightforward extension of 2D counterpart. The various steps for computer implementation are as follows

Step 1:

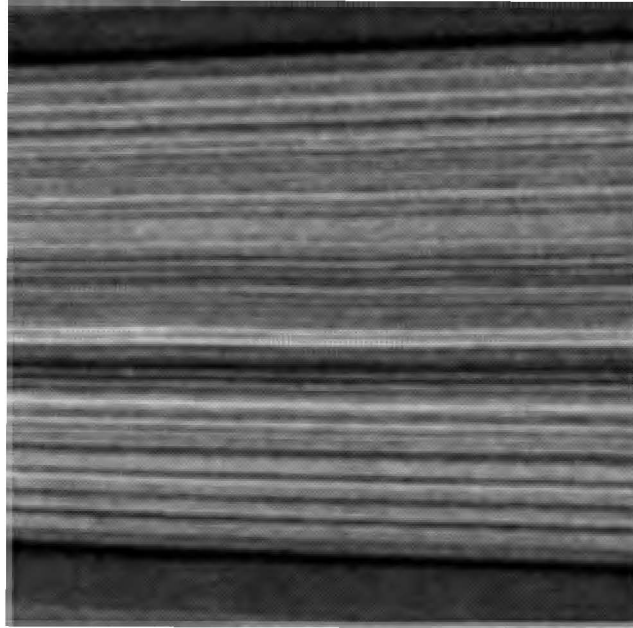
The first step is to obtain 2D projections $R_{\beta_i}(na, ma)$ from $G_{\beta_i}(na, ma)$ using equation 4.10 Data is sampled at sampling interval a in both the dimensions. This is because the CCD pixel elements in the camera are square. n and m take integer values with $(0,0)$ corresponding to the top left corner of the projection; β_i are the angles for which cone beam projections are known.

Step 2:

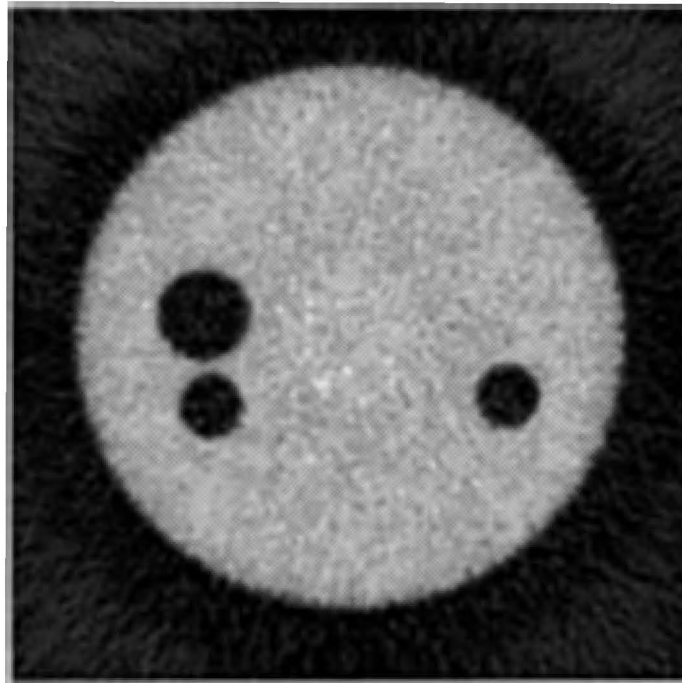
The next step is to generate for each cone beam projection $R_{\beta_i}(na, ma)$ the corresponding modified projection $R'_{\beta_i}(na, ma)$ given by equation 2.71

Step 3:

Smooth each row of modified projection $R'_{\beta_i}(na, ma)$ with smoothing filter $k(na)$.



(a)



(b)

Figure 4.11: (a) Image after 1 Backprojection (b) Final image 320 backprojections

Step 4:

Convolve each row of modified projection $R'_{\beta_i}(na, ma)$ with $g(na)$ to generate corresponding filtered projection

$$Q'_{\beta_i}(na, ma) = R_{\beta_i}(na, ma) * g(na) \quad \forall m \quad (4.29)$$

Step 5:

Perform weighted backprojection of each row of filtered projection along the corresponding tilted fan as given by equation 2.69. The sum of all backprojections is the reconstructed 3D image

$$f(x, y, z) = \frac{2\pi}{K} \sum_{i=1}^K \frac{1}{U^2(x, y, \tilde{z}\beta_i)} Q_{\beta_i}(s', \tilde{z}) \quad (4.30)$$

where K angles θ_i are those for which fan projections are known. The transformed coordinates (p, q, z) are calculated for every pixel using equation 2.5. Using these, U , s' and \tilde{z} are calculated using equations 2.72, 2.73 and 2.74 respectively. The value of s' and \tilde{z} are used to find n' and m' respectively. Since the projection data is of size 640x480 (NTSC standard), the 3D image size chosen should $L \times L \times H$ where

$$H = L \cdot \frac{480}{640} \quad (4.31)$$

Then

$$\begin{aligned} n' &= s' \cdot \frac{640}{L} \\ m' &= \tilde{z} \cdot \frac{480}{H} \end{aligned} \quad (4.32)$$

Also, n' and m' may not be integers, in which case they are rounded off to the nearest integers. For each pixel, the contribution of corresponding $Q_{\beta_i}(n', m')$ is added after weighing it by $\frac{1}{U^2}(x, y, \tilde{z}\beta_i)$.

Performance Improvement

The poor quality of reconstructed image in Figure 4.11(b) can be accounted for largely by the noise in the data introduced by the imaging chain. However, there are also certain systematic errors introduced due to image intensifier and camera response which have to be removed.

Gray Scale Subranging

Most A/D converters have a zero-offset and a reference voltage associated with them. The reference voltage controls the range of signal that can be digitized and zero-offset determines the signal level corresponding to 0. The incoming signal can be amplified before digitizing it which effects the resolution in terms of mV/gray-scale. These parameters viz: gain, reference and zero offset are shown schematically in Figure 4.12. The NTSC-signal ranges from 0.054-0.714 Volts. Therefore, the zero-offset for the A/D converter should be 0.054 and reference voltage should correspond to digitization range of 0.66 Volts. This is shown in Figure 4.13(a) for DT2867 8-bit converter. The reference voltage can be reduced to digitize only a part of signal. The zero-offset can then be moved to digitize different parts of the signal which can be added together. This is called gray scale subranging. There is lower limit to the A/D reference value below which the accuracy of the converter decreases. With DT2867, a gain of 4 coupled with reference voltage of 0.33 Volts allows for 8 levels of gray scale subranging. This is shown in Figure 4.13(b). The 8-bit A/D converter with the resolution of 2.57 mV/gray-scale is now converted into a 11 bit A/D with resolution of 0.32 V/gray-scale. This results in decrease in quantization noise.

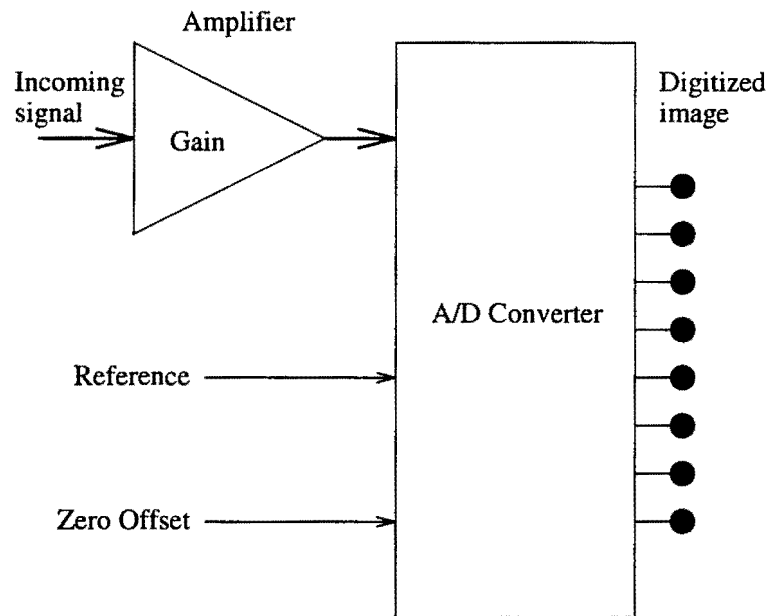
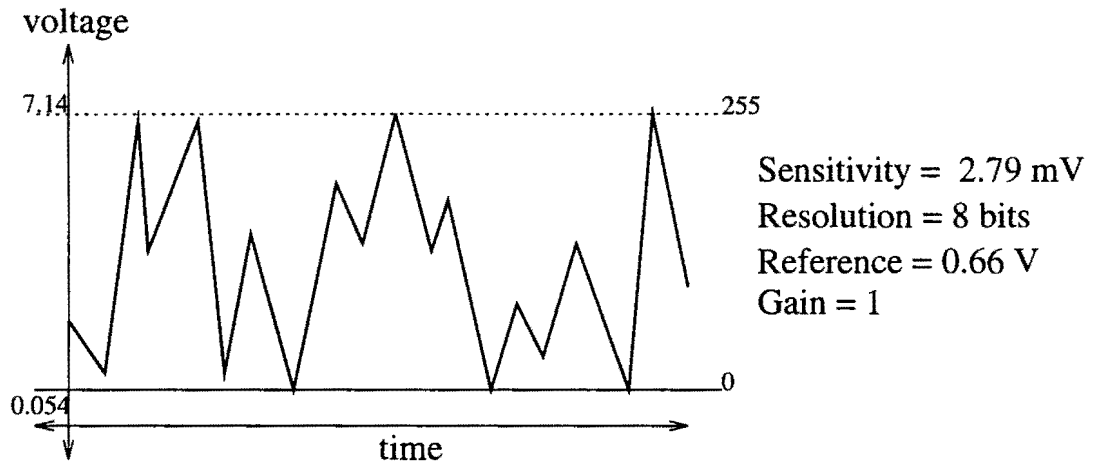


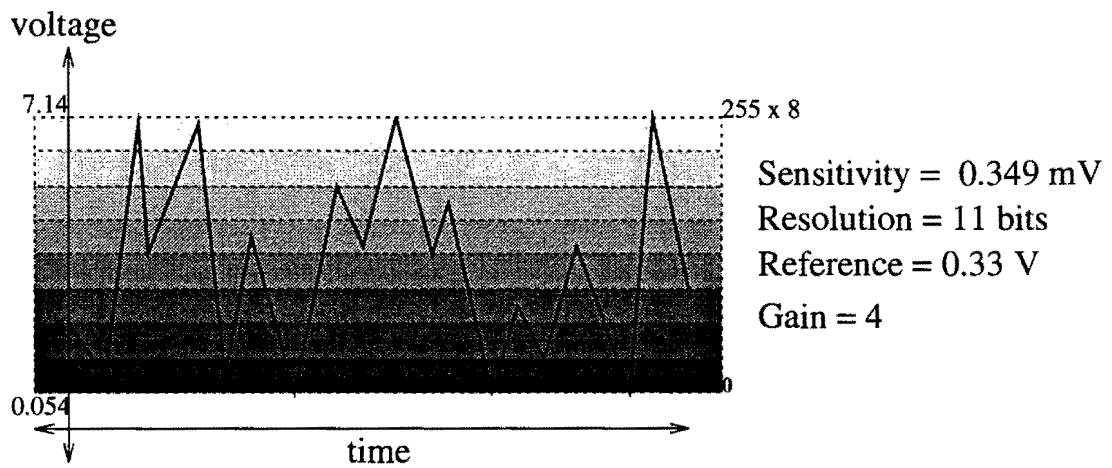
Figure 4.12: Simplified schematic of digitization process

Noise

The major source of noise is quantum mottle noise due to changes in the flux from the generator. Frame averaging can drastically reduce this noise. The 16-bit buffer on DT2867 can be used for fast accumulation of up to minimum of 256 frames. The projection data is read out of this accumulation buffer and floating point averaged. The integer arithmetic hardware on the DT2867 can be used for integer averaging which would roundoff noise in the image. Floating point averaging is therefore preferred. For comparison between the noise against the number of frames averaged, noise patterns are obtained by smoothing the slice of background and subtracting it from the original. Figure 4.14 shows a plot of the standard deviation of noise against the number of frames averaged. There is a dramatic decrease in the noise amplitude for initial few frames. After about 40-50 frames, the noise levels



(a)



(b)

Figure 4.13: Gray scale subranging

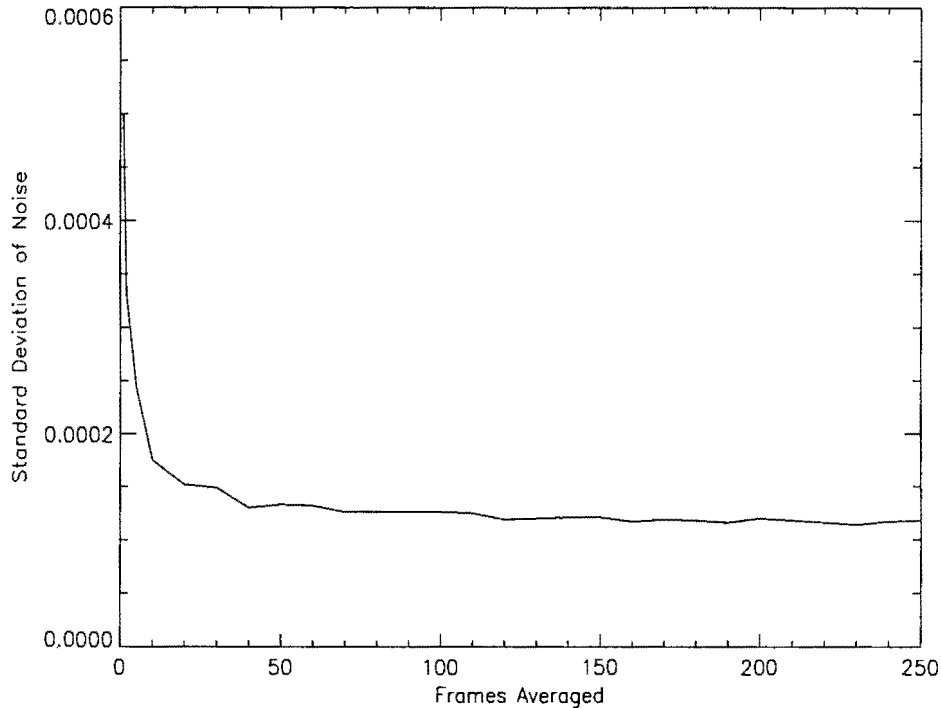


Figure 4.14: Noise against frames averaged

out. At the frame rate of 30 frames/second, it would take $N/30$ seconds to acquire one projection where N is the number of frames. Frame averaging has a tradeoff in terms of time required to collect each slice of data. Every 30 frames averaged add up to 6 minutes of data acquisition time if one is using 360 projections for reconstruction. Therefore, 40 frames is approximately an optimum number to average as there is no significant decrease in noise with further averaging.

Gray scale subbranging results in change in the shape of curve shown in Figure 4.14. Figure 4.15 shows the plot of noise amplitude against frame averaging for 1, 4 and 8 levels of subbranging. For comparison of the shapes, the standard deviation of noise is normalized with respect to that corresponding to one frame per

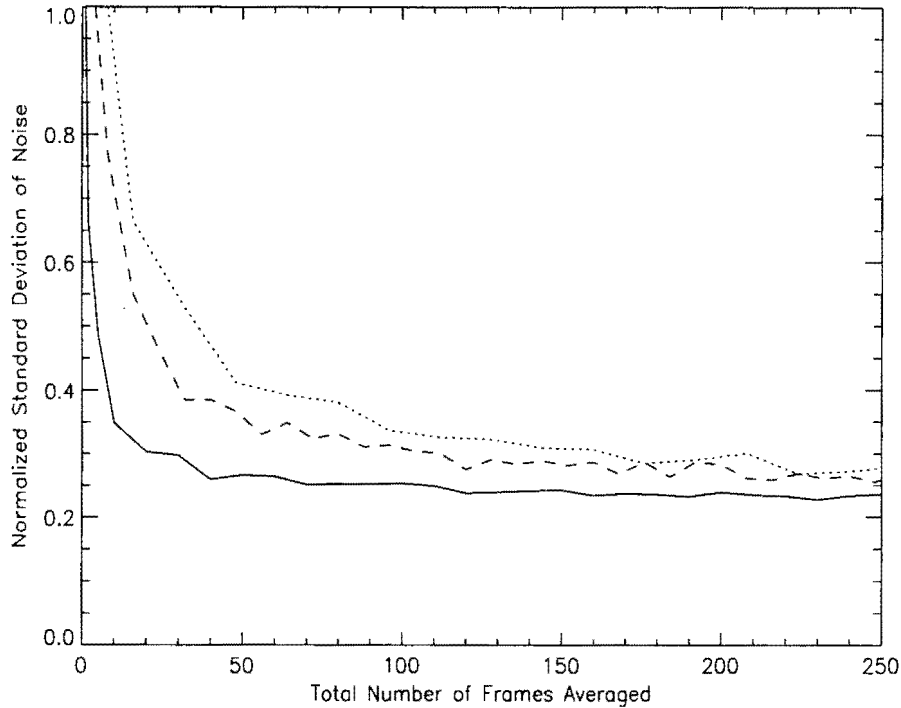


Figure 4.15: Noise against frames averaged for different levels of gray scale sub-ranging: 8(Dotted), 4(dashed), 1(Solid)

subrange. The noise takes more number of frames to level out with increase in number of subranges used. This is expected because each subrange would approximately take 40 frames averages to remove the quantum mottle.

Figure 4.16 shows the reconstructed image with 40 frames averaged for every projection.

Equalization

The imaging chain introduces certain systematic distortions in the data. The main indication of this is the shape of the background slice shown in Figure 4.17.

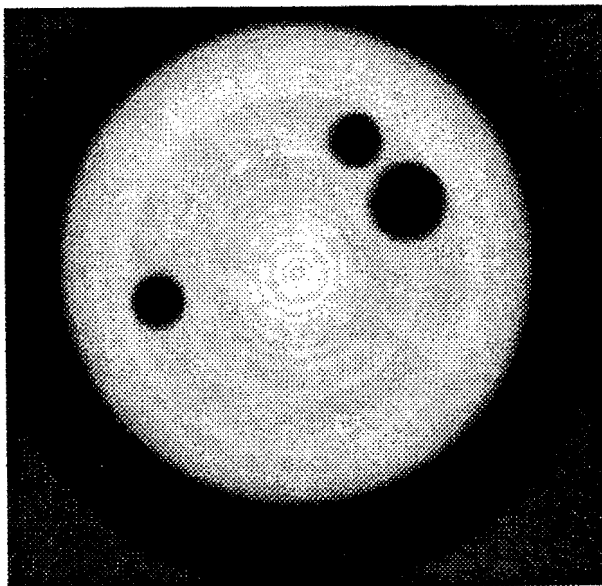


Figure 4.16: Reconstructed image after frame averaging

There is a gray scale intensity variation of as large as 20% across the slice. The radial divergence of the fan beam accounts for only a maximum of 2-3% change in intensity. Therefore, it can be concluded that the nonuniform electromagnetic focusing of the image intensifier is responsible for such a large change in the intensity levels. The focusing results in a more intensified image at the center than towards the edges. There is also a noticeable kink in the center of the slice. This can be due to defect in the phosphor coating on the face plate of image intensifier.

Many such background slices were taken at the same location with maximum frame averaging (256) to eliminate most of the random noise. So we are in the leveled part of the noise to number of frames averaged curve in Figure 4.14. The noisy pattern which rides on these slices is isolated using technique shown in Figure 4.17. Some of these patterns are shown in Figure 4.18. These are offset from each other

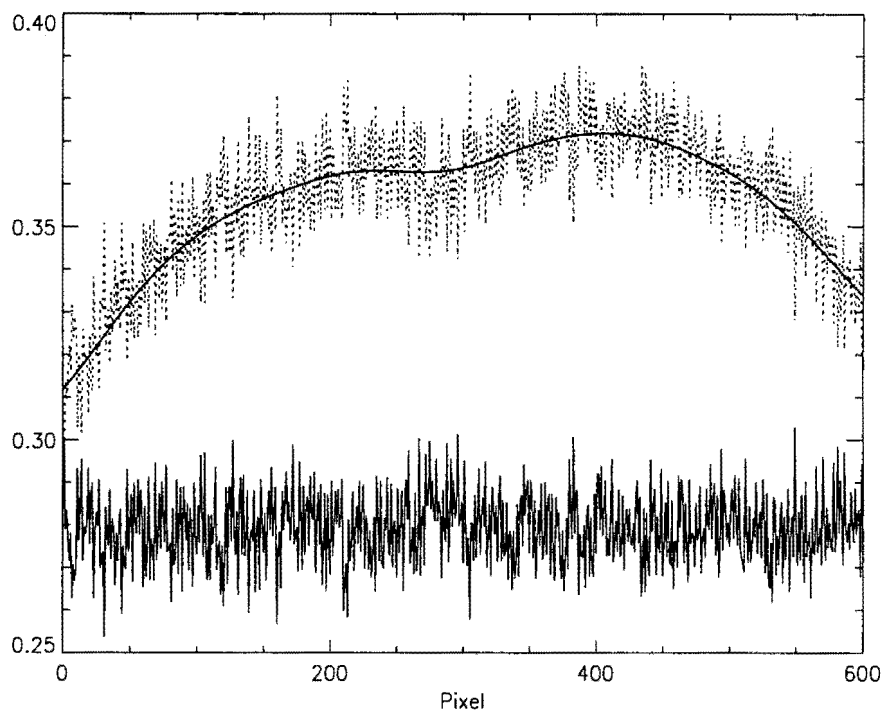


Figure 4.17: Dotted line is the background slice; Solid line passing through it shows the smoothed slice; Other solid line shows noise pattern which is offset for ease of viewing

for comparison. It can be seen that the patterns are very similar. They exhibit a very high of correlation between these patterns $\approx 0.95-0.99$. This suggests that this pattern is not random noise but represents changes in response of individual CCD elements of the camera. These small changes get repeated for every projection in the sinogram and when backprojected results in ring artifacts. These artifacts are clearly visible in reconstructed image in Figure 4.16. They are masked by random noise in Figure 4.11(b).

The gray level at a pixel for the x-ray flux depends on following factors:

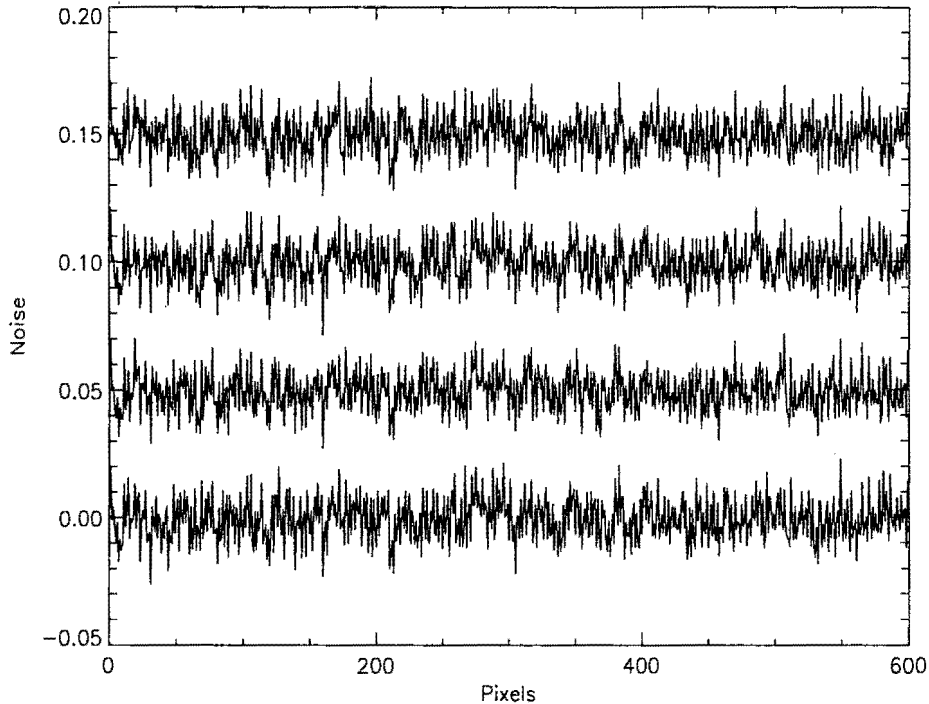


Figure 4.18: Patterns representing CCD noise

1. Variations in response of input phosphor screen to same x-ray flux.
2. Electromagnetic focusing of secondary electrons during minification.
3. Difference in individual characteristics of CCD elements in camera.

The pixel response characteristics for individual pixels is obtained by plotting the gray scales against the generator flux. Generator flux can be varied by either changing the voltage or the current. Figure 4.19 shows the same background slice for varying current and a constant tube voltage of 100 KV. The gray scales are obtained after integrating total of 256 frames. The characteristics of a few pixels are plotted in Figure 4.20. This plot normalized in both x and y axes. It can be seen that the characteristics are not linear. They will differ if any elements in the imaging chain

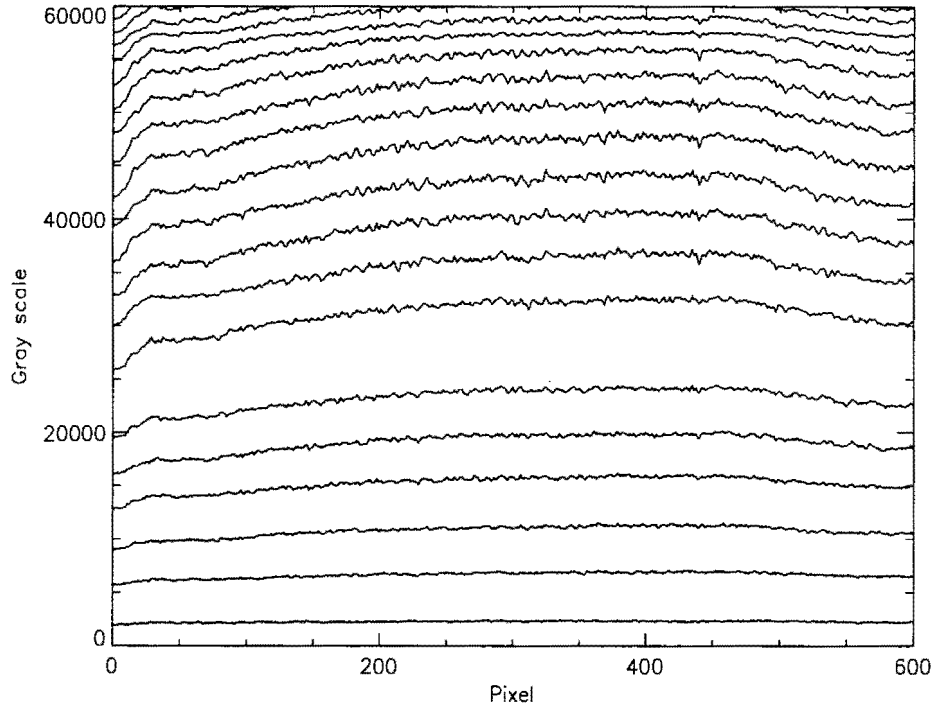


Figure 4.19: Background slices used for pixel response characterization

is changed or with aging, especially that of image intensifier. These characteristics are fitted with parametric curves. Here, a quadratic fit is found for each pixel using linear least square method. Hence, each pixel element i , there corresponds a_i , b_i and c_i such that

$$y_i = a_i x^2 + b_i x + c_i \text{ for } i = 0 \dots 640 \quad (4.33)$$

We find the average response

$$y = a_{av} x^2 + b_{av} x + c_{av} \quad (4.34)$$

where

$$a_{av} = \frac{\sum_{i=1}^{640} a_i}{640}$$

$$b_{av} = \frac{\sum_{i=1}^{640} b_i}{640}$$

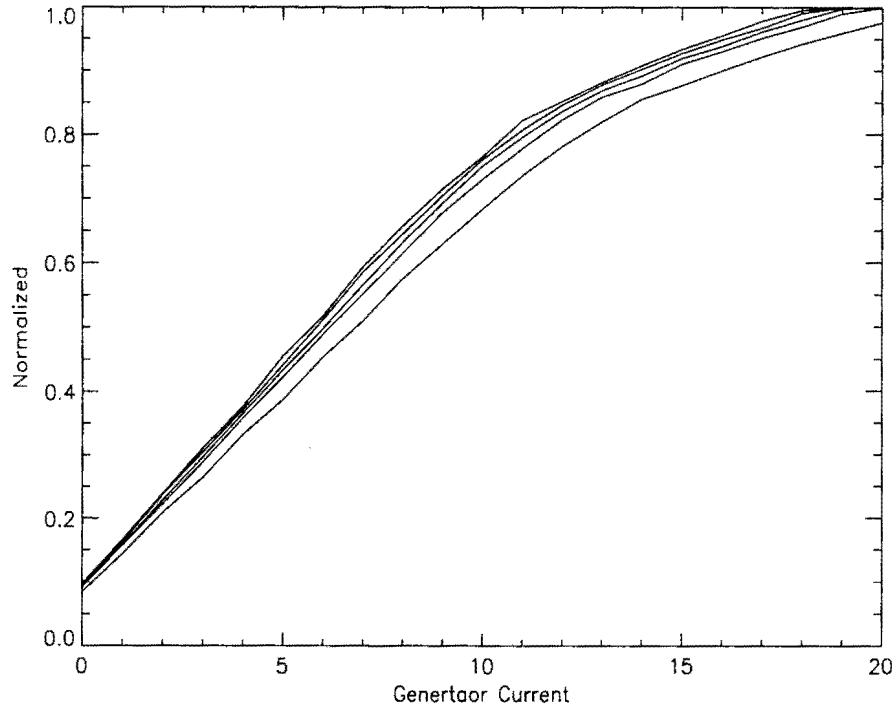


Figure 4.20: Pixel response characteristics plotted for pixel numbers 10, 100, 250, 400, 550, 630

$$c_{av} = \frac{\sum_{i=1}^{640} c_i}{640}$$

For a particular pixel i and gray scale y , we determine corresponding x using equation 4.33 and use it to calculate equalized gray scale y_e using equation 4.34.

The reconstructed image with this equalization is shown in Figure 4.21. It can be seen that as compared with Figure 4.16 the ring artifacts have considerably reduced.

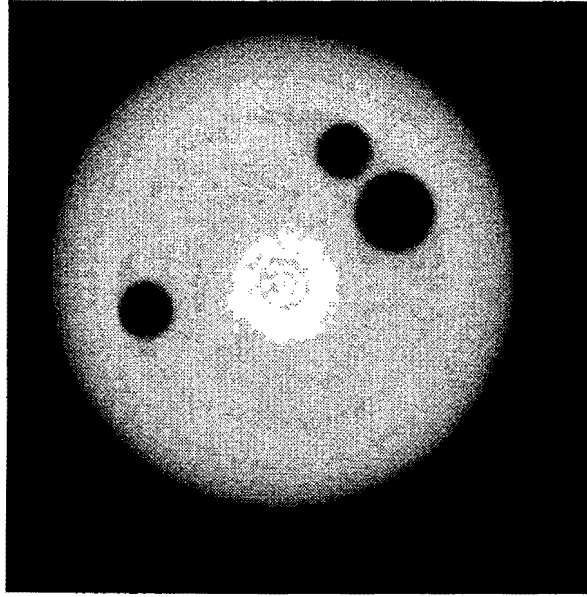


Figure 4.21: Reconstructed image after pixel response equalization

Smoothing

The backprojection kernel $g(na)$ is a high pass filter which magnifies even the slightest amount of noise in the projection. The filtered projection without any smoothing of data is shown in Figure 4.22(a). The high frequency component introduced due to the edges of the object swamp the rest of the data. A hamming window is used for smoothing. Figure 4.22 shows the sequence of filtered projection for increasing size of the window. The corresponding reconstructed images are shown in Figure 4.23. Hamming window of size 0, 4, 10 and 20 is used. The images look cleaner with increased smoothing but one has to pay in terms of the blurring introduced.

Convolutions are implemented by taking the Fourier transform of the two sequences and finding the inverse transform of their product. The Fast Fourier Trans-

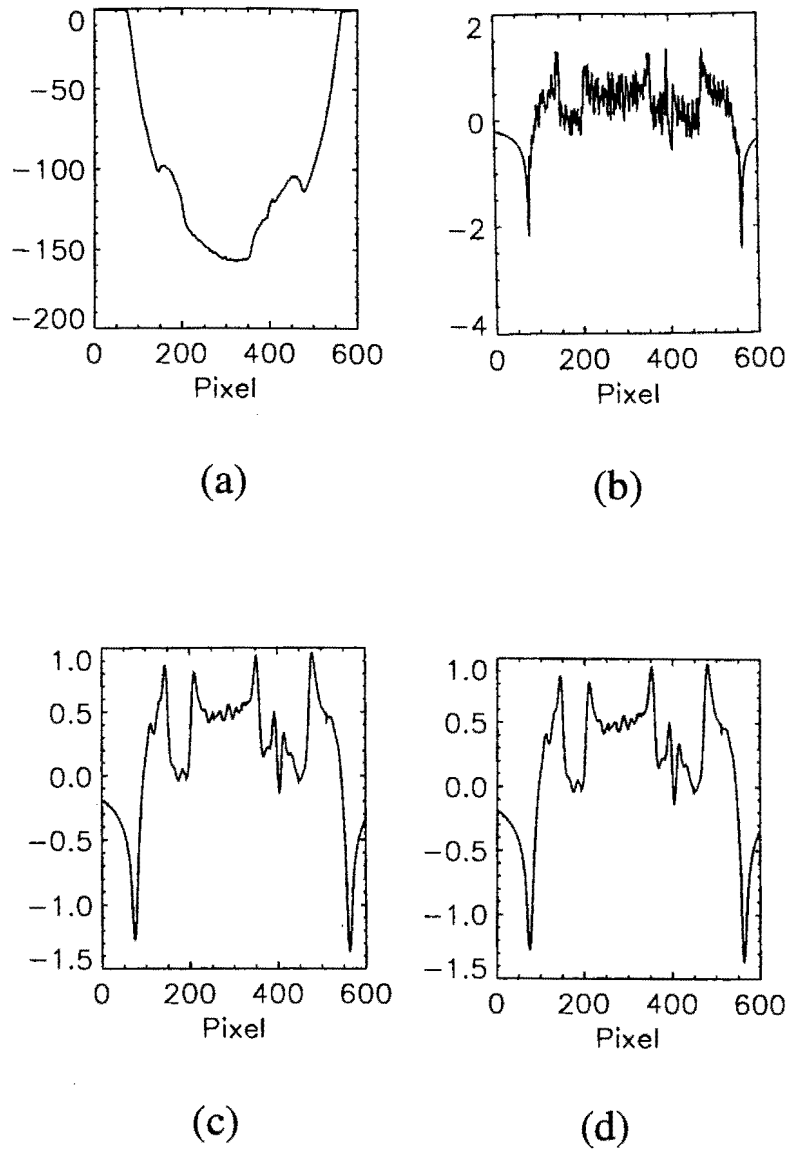
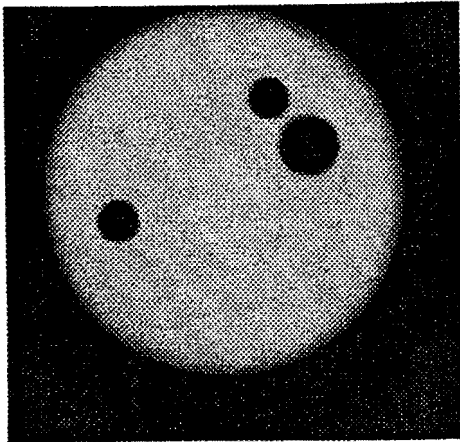
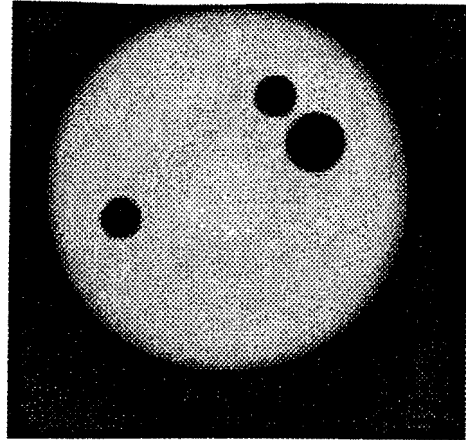


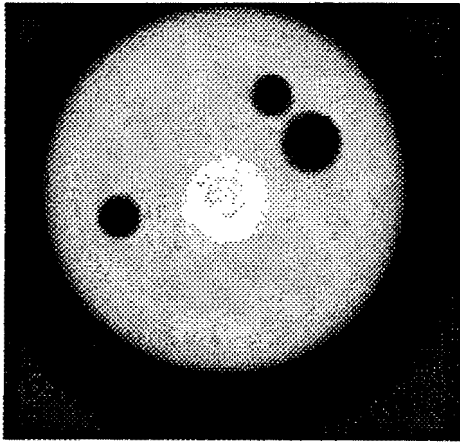
Figure 4.22: Filtered projections after varying choice of hamming window for smoothing (a) none (b) 4 (c) 10 (d) 20



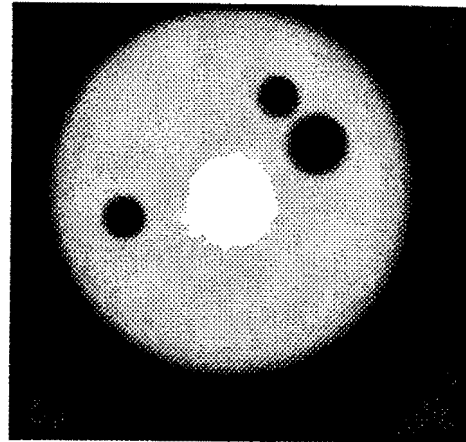
(a)



(b)



(c)



(d)

Figure 4.23: Reconstructed images after varying choice of hamming window for smoothing (a) none (b) 4 (c) 10 (d) 20

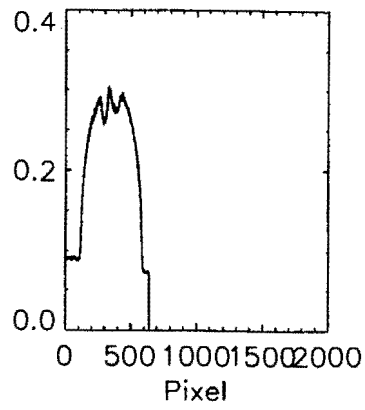
form algorithm used is decimation in time or frequency. The projection, which consists of 640 elements is zero padded to get sequence of length $2^{11} = 2048$ to avoid aliasing [7, 13]. If the projection does not contain zero values at its edges such as shown in Figure 4.24(a), zero padding introduces high frequency components in the filtered projection as shown in Figure 4.24(b) which overshadow the actual data. To avoid this, the two edges of the projection are joined together by a smooth line as shown in Figure 4.24(c). The corresponding filtered projection is shown in Figure 4.24(d).

Polychromaticity

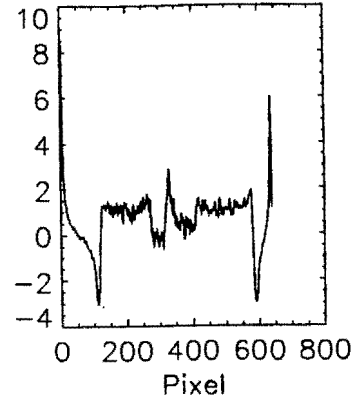
All the calculations done earlier were under the assumption that x-ray beam consists of monoenergetic photons. In practice, the generators emit a wide spectrum of x-rays called the bremsstrahlung spectrum. A sample of this spectrum is shown in Figure 4.25. The attenuation coefficient of materials also varies with x-ray energy. Most of the low energy x-rays are usually very quickly absorbed by material. Since, the image intensifier output is proportional to the x-ray flux incident on it, the object appears denser near the surface. It also results in artifacts which usually appear as dark streaks also known as beam hardening artifacts.

The beam hardening effect can be reduced by filtering the x-ray beam. This drastically reduces the lower energy x-ray photons. The output spectrum of a x-ray beam filtered with an 1mm Cu and 0.5mm Al filter is shown in Figure 4.26.

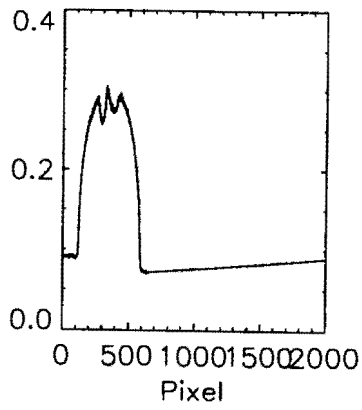
Other methods of removing beam hardening artifacts are: 1) preprocessing of the projection data, 2) postprocessing of the reconstructed image and 3) dual energy imaging. [9]



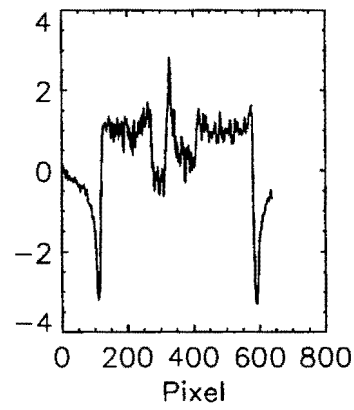
(a)



(b)



(c)



(d)

Figure 4.24: (a) Projection with zero padding (b) Filtered projection after zero padding (c) Projection with smooth padding (d) Filtered projection after smooth padding

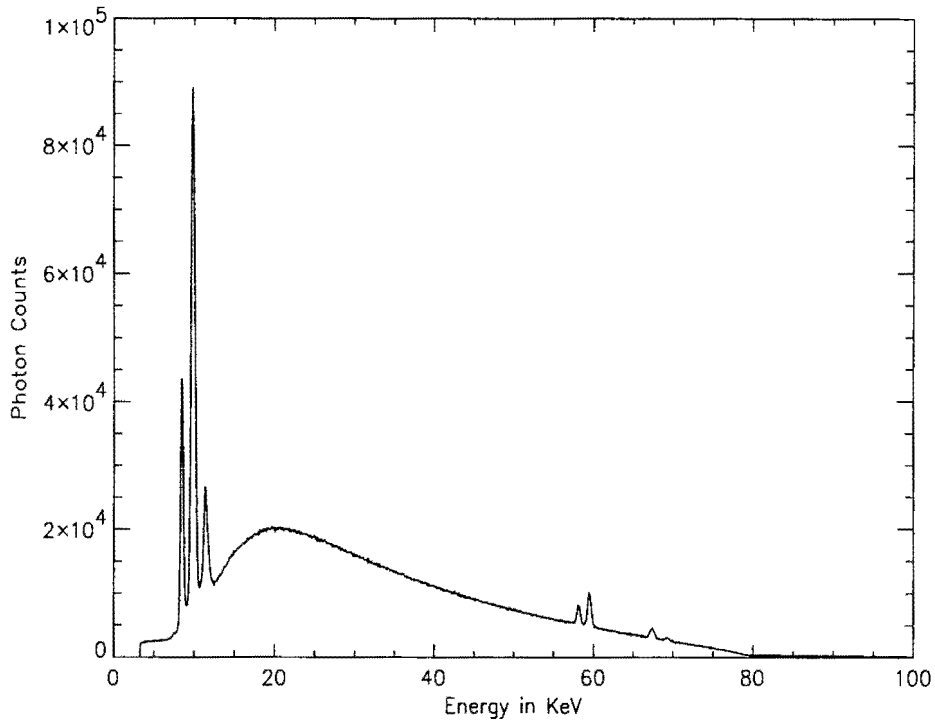


Figure 4.25: Bremsstrahlung spectrum from a X-ray generator

Also there is energy dependence of the image intensifier [6]. This results in the pixel characteristics shown in Figure 4.20 to vary for different spectra of x-ray flux incident on the image intensifier which explains the residual ring artifacts.

Implementation Flow

Figure 4.27 lists the steps that go into a typical tomographic scan. The foremost step is align the object properly so that it occupies the field of view. This can be done very conveniently using the real time system software XR-VISION [24] and the sample positioner control. There is also a facility for observing a real time slice of the

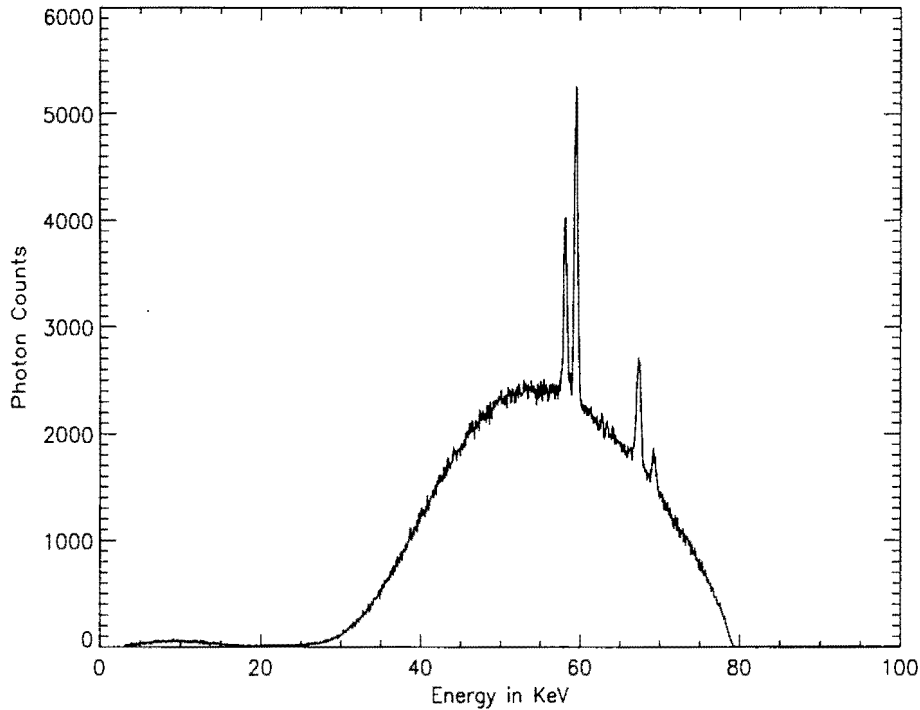


Figure 4.26: Spectrum of filtered beam from a X-ray generator

projection as the object is rotated. This helps in quickly ascertaining the generator settings (kilovoltage and current) such that there is no missing data in any of the projections i.e. there should not be substantial amount of saturation or cutoff for the projections through the object. Abrupt saturation or cutoff causes high frequency components to be introduced and results in streaks across the reconstructed image. The system initialization parameters such as I/O addresses and scan parameters such as number of projections to be taken, number of frames to be averaged, distances involved, speed of motor etc are read from a configuration file. The COR is determined using the appropriate object usually mounted on the object to be inspected (which sometimes is itself used). The rotation stage is revolved with a high set ve-

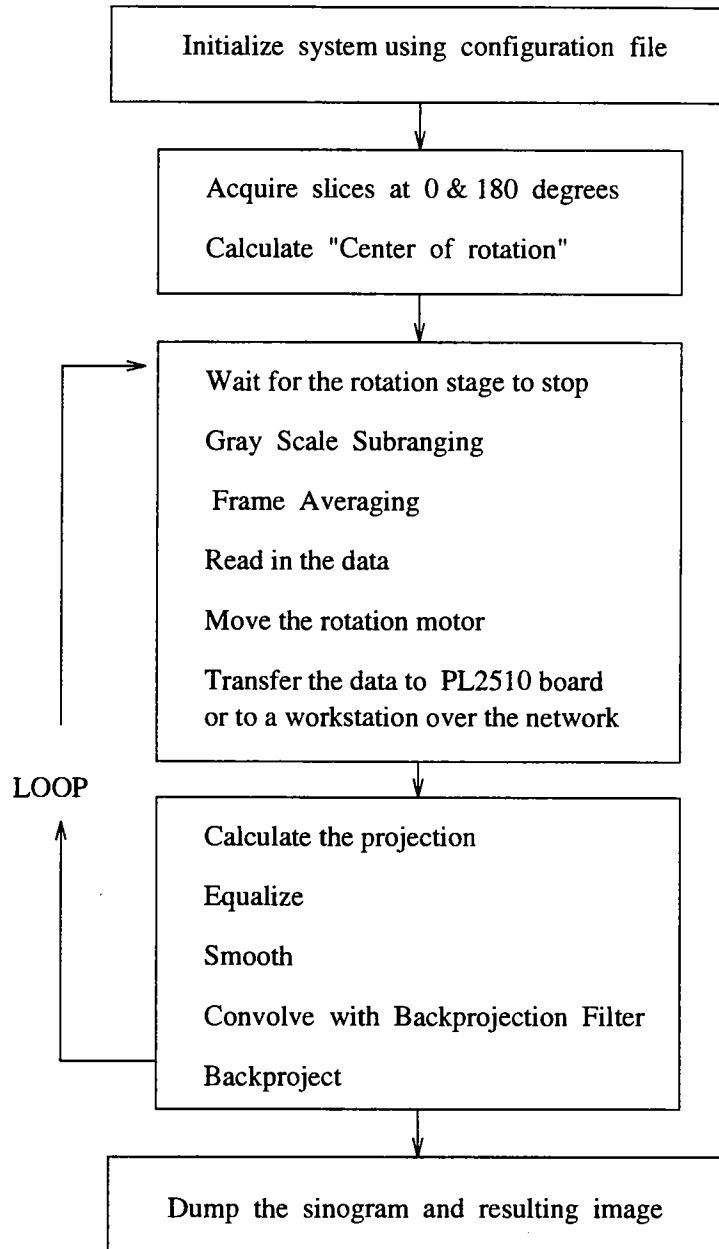


Figure 4.27: Flowchart

locity during this step. The data acquisition consists of frame averaging and gray scale subranging on the frame grabber. Command to move the motor is given at this point. Meanwhile, the digitized image is read out from the accumulation buffer. This constitutes the data acquisition part.

There are several options for reconstruction. Simplest would be to store the sinogram and then reconstruct the image. There is also a reconstruction program implemented on the array processor PL2500. The 1Meg memory on this board allows for 256x256 backprojection image plane. There is also a facility for transferring the data onto a workstation over the network connection [10, 14]. Reconstruction is done on the workstation. However, the last method is the only practical option when 3D reconstruction is to be done. Each projection would occupies 600K and storing say typically 180 such projections would very quickly fill up hard disks. Therefore, reconstruction must be done on the fly with data acquisition. The large amount of memory required for a 3D backprojection image plane and volume of computation involved make it imperative to use the power of workstation.

Typically, a 2D tomographic scan takes 15 minutes where 180 projections are used. The time is essentially limited by data acquisition. The 3D scan takes however takes 3 hours using a single machine. There is a potential for distributing the reconstruction load over the network and get achieve speed comparable to that of 2D scan.

Source code for reconstruction algorithms and various other utilities is given in [25].

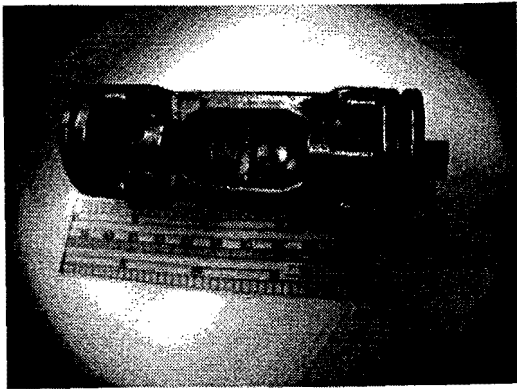
CHAPTER 5. RESULTS

In this chapter, we will discuss applications of the system developed pertaining to work being done at Center for Nondestructive Evaluation, Iowa State University. It is aimed towards demonstrating the practical viability of the project.

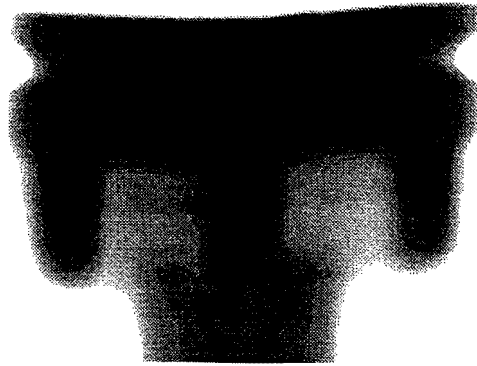
Casting Inspection

Metal castings suffer from porosity. Due to the surface texture and complexity of the part geometry, this problem is conducive for X-ray inspection. As an example, a casting used in automobile air conditioner is shown in Figure 5.1(a). Here, porosity or voids are unacceptable if they lie close to the any surface or if they are over a certain size. A real time inspection quickly brings out a large void located towards one end of the part as shown in Figure 5.1(b). A tomographic scan is done at that location and the reconstructed image is shown in Figure 5.1(c). The geometry and the location of the void can be clearly ascertained. Also, a small amount of porosity can be seen. One can therefore envisage a real time inspection system for castings where if there is doubt about the defect location or size, a quick tomo scan can be done that point to get complete information about it. This would result in fewer rejected parts.

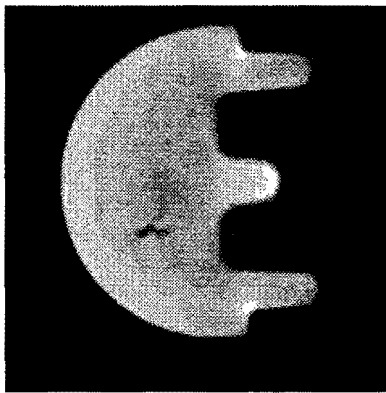
A 3D tomogram of the sample was obtained. Figure 5.2 shows the sequence of



(a)



(b)



(c)

Figure 5.1: (a) Aluminum casting (b) Image from the realtime system (c) Reconstructed image

slices at equal intervals in the reconstructed 3D image.

Inspection of Cracks

Figure 5.3(a) shows a aluminum bar with a fatigue crack induced by low cycle high load. The real time image of the crack is shown in Figure 5.3(b). It gives a very good idea lateral idea about the crack but is not capable of providing a good view along the length of the crack inside the sample. Tomographic scan of a slice near the bottom of the crack is shown in Figure 5.3(c). We zoom onto the crack with some contrast enhancement in Figure 5.3(d). There is a very obvious fork seen at one end of the crack.

The 3D reconstruction of this sample gives a very complete information about the fatigue crack as it propagates into the material. Slices of the 3D image are shown in Figure 5.4. This demonstrates the capability of this system to provide complete information about the geometry of the flaws.

Packing Density

Images reconstructed using tomographic scans across rock samples of different sizes in a glass vial are shown in Figure 5.5. Difference in the packing density are clearly visible as the size of rock particles decreases. This is a precursor to a more ambitious project of determining the differences in packing density of fibers in green state ceramic composites. This will help in analyzing the various techniques of manufacturing them. The major issue here is accurately aligning the axis of rotation perpendicular to the x-ray fan plane since the fibers are only about a tens of microns in diameter.

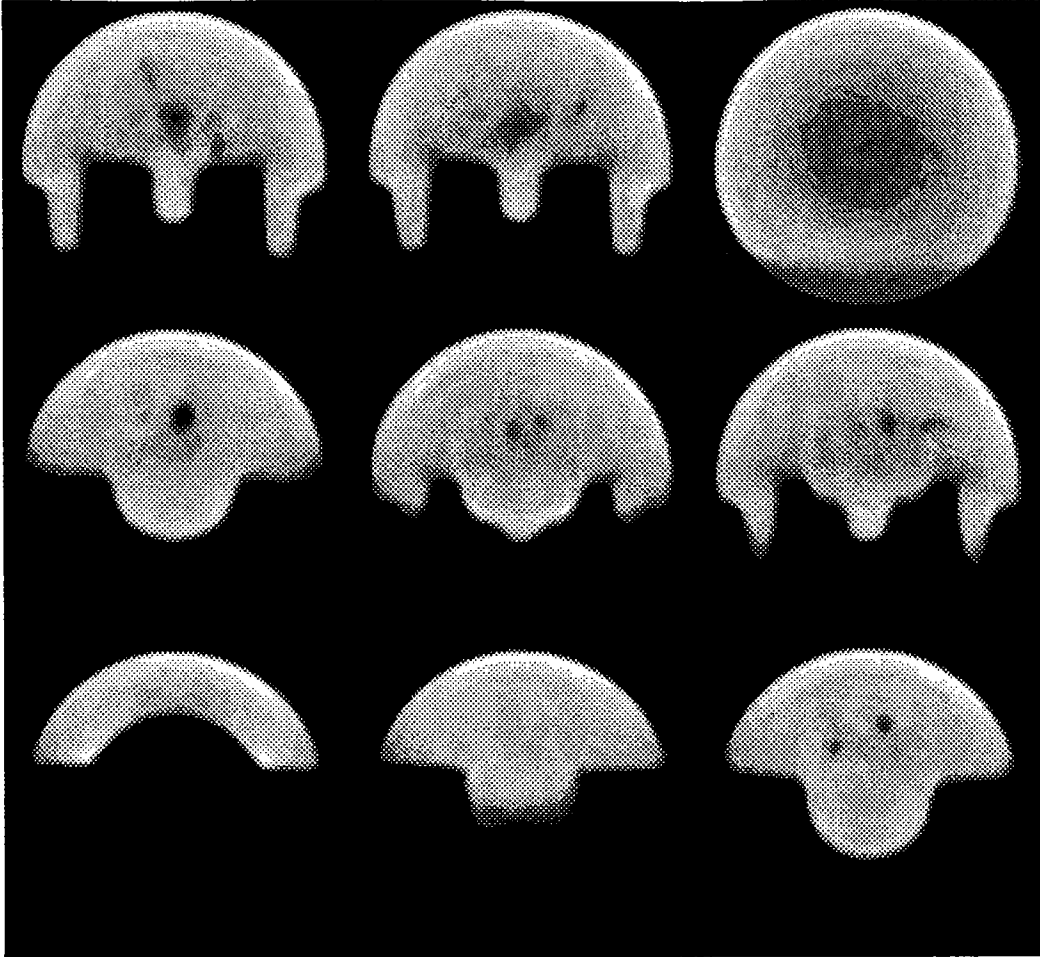


Figure 5.2: Slices across a 3D tomogram of aluminum casting

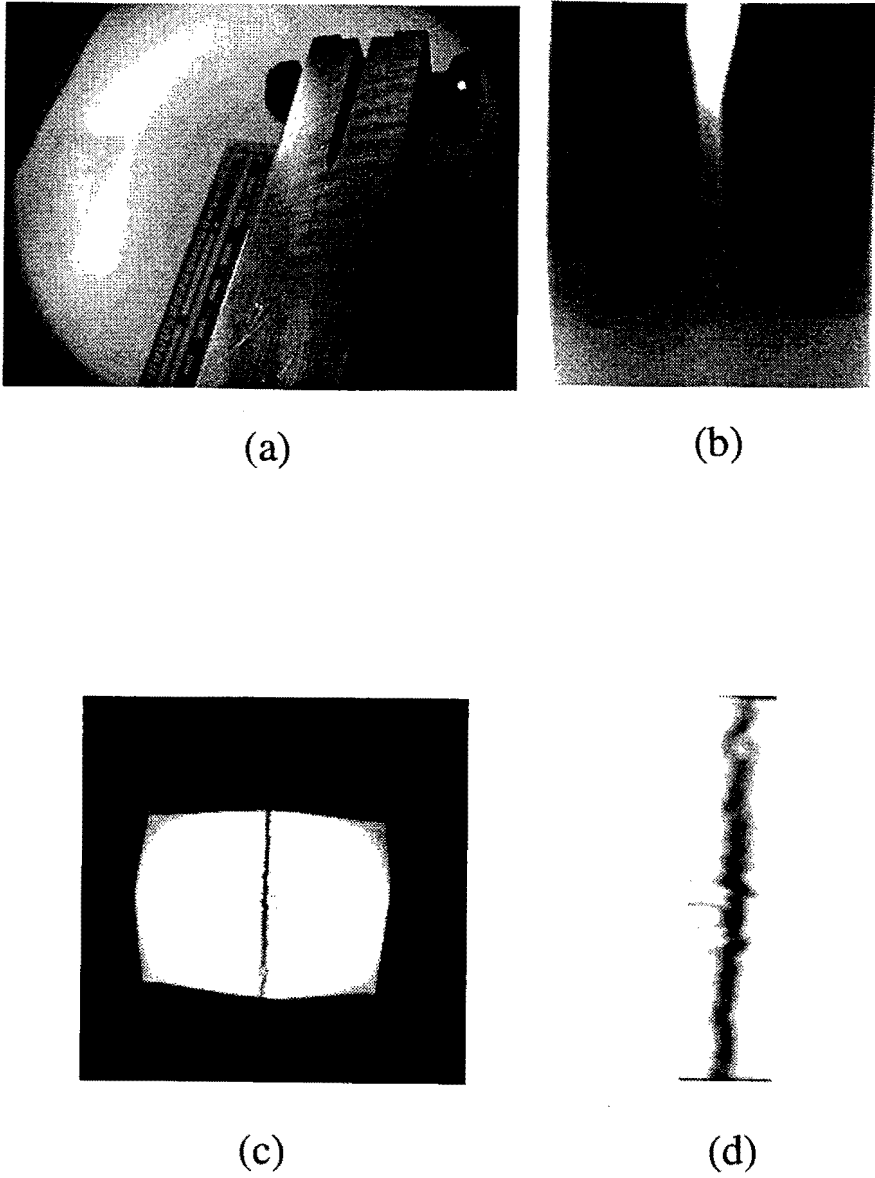


Figure 5.3: (a) Fatigue crack sample (b) Image from the real-time system (c) Reconstructed image (d) Crack (zoomed)

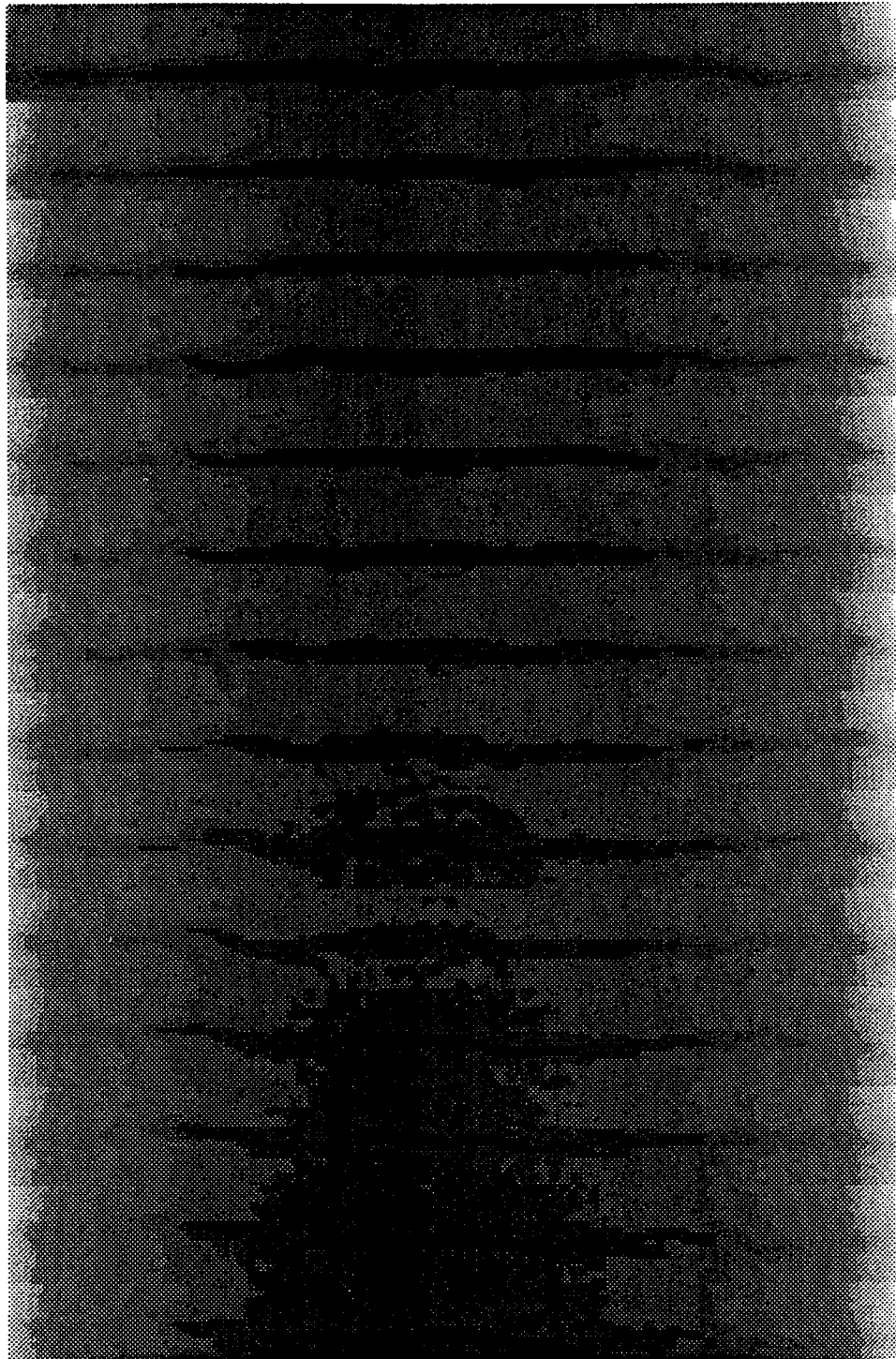
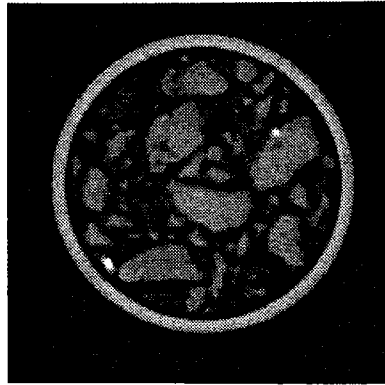


Figure 5.4: Slices across a 3D tomogram of fatigue crack



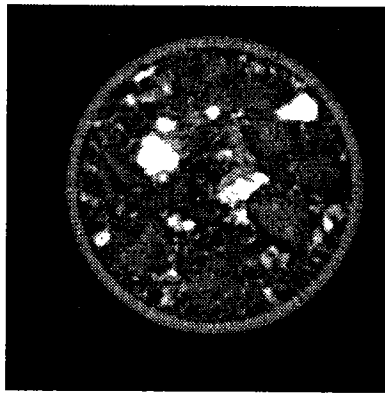
(a)



(b)



(c)



(d)

Figure 5.5: Slices across rock samples with different packing densities

CHAPTER 6. CONCLUSIONS AND FUTURE WORK

Conclusions

Traditionally, CT systems are very expensive because they were primarily used for medical applications. There were stringent constraints in terms of speed of data acquisition to avoid overexposure of patients to the radiation and volume and complexity of the calculations involved in reconstruction algorithm required custom hardware for obtaining quick results. There are now powerful industrial CT inspection systems which have fast throughput and good image quality. The detectors and hardware costs escalate the total cost of such system to millions of dollars. We are not competing with such expensive systems. The result of this thesis is essentially a *poor man's CT*. Given that a person has a barebones of a real time x-ray inspection(generator, image intensifier and television monitor), with additional equipment of \approx \$25000, he can have a CT capability (poor is a relative term). The image quality using the raw data is bad but it can be greatly improved by the techniques presented in this thesis. For the CT system developed here, Figure 4.11(b) and 4.21 show this improvement. If need be, postprocessing can be applied to reconstructed images to enhance them and remove artifacts such as ringing.

Implementation of backprojection algorithm requires efficient handling of available memory and repetitive code for better speed. Tweaking the parameters such as

the size of the smoothing window can change the final image quality. The speed for our system is essentially limited by the data acquisition time.

3D tomographic inspection is a very powerful tool since it provides almost complete information of the object. The system is capable of fast 3D reconstruction using distributed processing. However, there are powerful DSP boards available which can be used to handle the volume of computations involved.

Future Work

Dynamic Range Expansion

The major limitation of the tomographic inspection system implemented here is the low dynamic range of the image intensifier. This could be improved by changing the generator output flux (by changing kilovoltage and current settings) and collecting several images. These can be added up appropriately to get a single high dynamic range image. The major hurdle here is making an accurate model of the image intensifier response for various X-ray spectra and relating the X-ray spectra emitted by the generator to kilovoltage and current settings [6, 23]. Also, it would be necessary to determine the changes in these models over time and especially the change in generator model with cathode filament replacements. Another approach would be to use a higher bit camera and digitizer, in which case, the cost escalates rapidly.

Inspecting Objects Larger than Field of View

For obtaining high spatial resolution, it becomes necessary to go for very high magnification. However, with higher magnification, the field of view decreases. to achieve spatial resolution in tens of micron, the field of view becomes as small as a

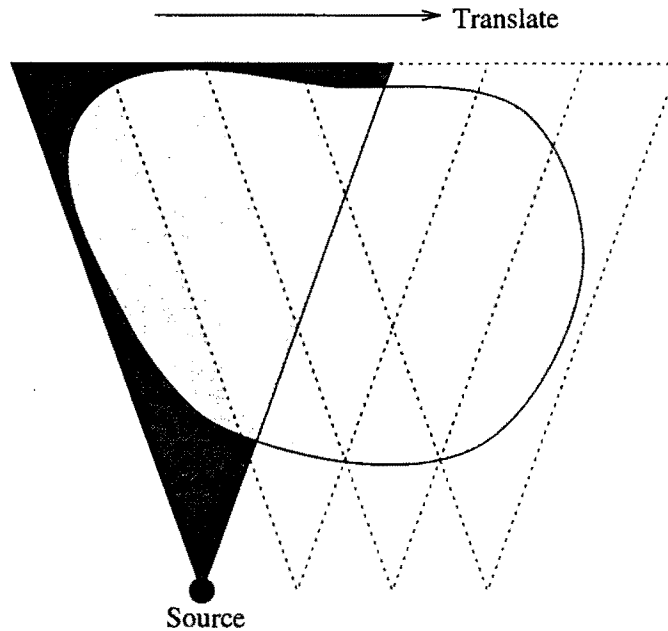


Figure 6.1: Inspecting objects larger than field of view

millimeter. Such a situation can also arise when the object to be inspected is large and exceeds the field of view even at low magnification. In such cases, one can acquire several projections by translating the object as shown in the Figure 6.1 and then put these together to form one single projection. The problem here is the way to put these fan projections together.

Camera Mount

The camera in the present system is mounted and focused manually (very laborious procedure). This does not give the any freedom to the adjust the focus or zoom during the actual inspection. It would be ideal to have a motorized and remotely controlled camera focus and zoom adjustments. This would enable quick and accurate focusing. Also, the facility to zoom onto any part of the image would improve

the effective spatial resolution.

Distributed 3D Reconstruction

The 3D cone beam reconstruction is as of now implemented on a single workstation. This makes the reconstruction time a dominating factor in determining the total time taken to do 3D CT. However, this task can be distributed over the several machines with each machine responsible for processing and backprojecting $\frac{480}{T}$ slices of data where T is the number of machines used. The inspection time in such a case would be again dominated by the data acquisition as in 2D reconstruction. Quick 3D inspections are a very attractive proposition.

Integrated System

The X-ray CT simulation, actual CT inspection (2D and 3D) and visualization of the system can be put together into one powerful integrated package. The data acquisition can be done in a distributed fashion with the PCs and the packaged program can be executed on any workstation or even a powerful PC.

BIBLIOGRAPHY

- [1] J.Radon. *Über die Bestimmung von Funktionen durch ihre Integralwertelangs gewisser Mannigfaltigkeiten*. Berichte über die Verhandlungen, Vol. 69, p. 262, 1917.
- [2] Lewis S. Edelheit, Gabor T. Herman, and Arasanipalai V. Laxminarayanan. *Reconstruction of objects from diverging x-rays*. Med Phys., Vol. 4, No. 3, May/June 1977
- [3] Carl R. Crawford, and Grant T. Gullberg. *Reconstruction for fan beam with an angular-dependent displaced center-of-rotation*. Med Phys., Vol.15, No.1, Jan/Feb 1988
- [4] David C. Copley, Jeffery W. Eberhand, and Gregory A. Mohr. *Computed Tomography Part I: Introduction and Industrial Applications*. JOM, Jan 1994
- [5] Gregory L. Hoeft, Simon H.C, and Robert E. Slocum. *Low cost computed tomography system using an image intensifier*. SPIE Vol.1396 Applications of Optical Engineering: Proceedings of OE/Midwest'90
- [6] Sarat Kakumanu, *M.S. Thesis*. Department of Electrical Engineering, Iowa State University, Ames, Iowa. Fall-1994

- [7] Alan V. Oppenheim, and Ronald W. Schaffer. *Discrete-Time Signal Processing*. Prentice Hall, Englewood Cliffs, New Jersey. 1989
- [8] Rafael C. Gonzalez, and Paul Wintz. *Digital Image Processing*. Second Edition. Addison Wesley, Reading, Massachusetts. 1977
- [9] Avinash C. Kak, and Malcolm Slaney. *Principles of Computerized Tomographic Imaging*. IEEE press, New York, c1988
- [10] W.Richard Stevens, *Unix Network Programming*. Prentice Hall Software Series, Englewood Cliffs, New Jersey. 1990
- [11] Bjarne Stroustrup, *The C++ Programming Language*. Second edition, Addison-Wesley Publishing Company, Reading, Massachusetts. 1991
- [12] Csorba, I. P. *Image tubes*. Howard W. Sams and Co., Indianapolis, Illinois. 1985
- [13] William H. Press, Brian P. Flannery, Saul A. Teukolsky and William T. Vetterling. *Numerical Recipes in C - The art of scientific computing*. Cambridge University Press, The Pitt Building, Trumpington Street, Cambridge, U.K. 1988
- [14] *WINSOCK Reference Manual*. Public Domain Microsoft Windows socket library, X-ray Group, Center for NDE, Ames, Iowa. 1994
- [15] *Operation and Maintenance Manual IRT64050-A01*. IRT Industrial X-ray Systems, 3030 Callan road, San Diego, California. 1990
- [16] *Operating Instructions Manual*. FeinFocus X-ray Units, Leybold Inc., 1860, Hartog Drive, San Jose, California. 1990

- [17] *PC23 Indexer User Guide*. Compumotor Division of Parker Hannifin Corporation, 5500 Buisness Park Drive, Rohnert Park, California. 1992
- [18] *Positioning Control Systems and Drives*. Compumotor Digiplan 1992-93 Catalog, Compumotor Division, 5500 Buisness Park Drive, Rohnert Park, California. 1992
- [19] *C-Linda User's Guide & Reference Manual*. v.2.5.2, Scientific Computing Associates Inc., One Century Tower, 265 Church Street, New Haven, Conneticut. April 1993
- [20] *DT2867 Hardware & Software Manuals*. Data Translation Inc., 100 Locke Drive, Marlboro, Massachusetts. 1991
- [21] *Reference manual for PL series processor*. Eighteen Eight Laboratories, 1247 Tamarisk Lane, Boulder city, Nevada. Feb 1991
- [22] *PVWave Technical Reference Manual*. Precision Visuals, Inc., 6260 Lookout road, Boulder, Colorado. August 1990
- [23] Joe Gray, *XRSim: X-ray simulation*. X-ray Group, Center for NDE, Ames, Iowa. 1994
- [24] Richard Wallingford *XRVis: Real-tome x-ray inspection*. X-ray Group, Center for NDE, Ames, Iowa. 1994
- [25] Vivekanand Kini, *Source Code Book*. X-ray Group, Center for NDE, Ames, Iowa. July 1994.